

C/EBP α confers dependence to fatty acid anabolic pathways and vulnerability to lipid oxidative stress-induced ferroptosis in FLT3-mutant leukemia

Marie Sabatier^{1,2,3,*}, Rudy Birsén^{4,5,6,7,*}, Laura Lauture^{1,2,3,*}, Sarah Mouche^{4,*}, Paolo Angelino^{8,+}, Jonas Dehairs^{9,+}, Léa Goupille^{1,2,3}, Ismael Boussaid^{5,6}, Maël Heiblig^{10,11}, Emeline Boet^{1,2,3}, Ambrine Sahal^{1,2,3}, Estelle Saland^{1,2,3}, Juliana C. Santos¹², Marc Armengol¹², Miranda Fernández-Serrano¹², Thomas Farge^{1,2,3,26}, Guillaume Cognet^{1,2,3}, Federico Simonetta⁴, Corentin Pignon^{1,13}, Antoine Graffeuil^{1,13}, Céline Mazzotti^{1,13}, Hervé Avet-Loiseau^{1,13}, Océane Delos¹⁴, Justine Bertrand-Michel¹⁴, Amélie Chedru¹⁵, Vilma Dembitz¹⁶, Paolo Gallipoli¹⁶, Natasha S. Anstee^{17,18}, Sun Loo^{17,18,19}, Andrew H. Wei^{17,18,19}, Martin Carroll²⁰, Armelle Goubard²¹, Rémy Castellano²¹, Yves Collette²¹, François Vergez^{1,2,3,13}, Véronique Mansat-De Mas^{1,2,3,13}, Sarah Bertoli^{1,2,3,13}, Suzanne Tavitian¹³, Muriel Picard²², Christian Récher^{1,2,3,13}, Nathalie Bourges-Abella²³, Fanny Granat^{1,2,3}, Olivier Kosmider^{5,6}, Pierre Sujobert^{10,11}, Benoit Colsch¹⁵, Carine Joffre^{1,2,3}, Lucille Stuaní^{1,2,3}, Johannes V. Swinnen⁹, Hervé Guillou²⁴, Gael Roué¹², Nawad Hakim²⁵, Anne S. Dejean²⁵, Petros Tsantoulis^{4,8}, Clément Larrue⁴, Didier Bouscary^{5,6,7}, Jerome Tamburini^{4,5,6,#,§} and Jean-Emmanuel Sarry^{1,2,3,#,§}

¹Centre de Recherches en Cancérologie de Toulouse, Université de Toulouse, Inserm U1037, CNRS U5077, Toulouse, France

²LabEx Toucan, Toulouse, France

³Équipe labellisée Ligue Nationale Contre le Cancer 2018, Toulouse, France

⁴Translational Research Centre in Onco-hematology, Faculty of Medicine, University of Geneva, and Swiss Cancer Center Leman, Geneva, Switzerland

⁵Université de Paris, Institut Cochin, CNRS U8104, Inserm U1016, Paris, France

⁶Équipe Labellisée Ligue Nationale Contre le Cancer, Paris, France

⁷Assistance Publique-Hôpitaux de Paris, Hôpitaux Universitaires Paris Centre, Service d'Hématologie Clinique, Paris, France

⁸Swiss Institute of Bioinformatics, Lausanne, Switzerland

⁹Laboratory of Lipid Metabolism and Cancer, Department of Oncology, LKI - Leuven Cancer Institute, KU Leuven, 3000 Leuven, Belgium

¹⁰Hospices Civils de Lyon, Hôpital Lyon Sud

¹¹CIRI, Inserm U1111 CNRS 5308, Université Lyon 1, Lyon, France

¹²Lymphoma Translational Group, Josep Carreras Leukaemia Research Institute, 08916 Badalona, Spain

¹³Centre Hospitalier Universitaire de Toulouse, Institut Universitaire du Cancer de Toulouse Oncopole, Service d'Hématologie, Toulouse, France

¹⁴MetaboHUB-MetaToul, National Infrastructure of Metabolomics and Fluxomics, University Paul Sabatier, Toulouse, France

¹⁵Université Paris-Saclay, CEA, INRAE, Département Médicaments et Technologies pour la Santé, MetaboHUB, Gif sur Yvette, France

¹⁶Centre for Haemato-Oncology, Barts Cancer Institute, Queen Mary University of London, London, United Kingdom

¹⁷Walter and Eliza Hall Institute of Medical Research, Parkville, Australia

¹⁸Department of Medical Biology, University of Melbourne, Parkville, Australia

¹⁹Clinical Haematology, Peter MacCallum Cancer Centre & Royal Melbourne Hospital, Melbourne, Australia

²⁰Department of Medicine, Perelman School of Medicine, University of Pennsylvania, 715 Biomedical Research Building II/III, 421 Curie Boulevard, Philadelphia, PA 19104, USA

²¹Aix-Marseille Univ, Inserm, CNRS, Institut Paoli-Calmettes, CRCM, Marseille, France.

²²Centre Hospitalier Universitaire de Toulouse, Institut Universitaire du Cancer de Toulouse Oncopole, Service de Réanimation, Toulouse, France

²³CREFRE, Université de Toulouse, Inserm, ENVT, UPS, Toulouse

²⁴Toxalim (Research Centre in Food Toxicology), Université de Toulouse, INRAE, ENVT, INP-Purpan, University Paul Sabatier, Toulouse, France

²⁵Institut Toulousain des Maladies Infectieuses et Inflammatoires (INFINITY), Inserm UMR1291, CNRS UMR5051, Université Toulouse III, Toulouse, France

²⁶Present address: Institut des Maladies Métaboliques et Cardiovasculaires, Inserm/Université Toulouse III, U1297, Toulouse, France ; Institut Fédératif de Biologie, CHU Toulouse, Toulouse, France

*These authors equally contributed to this article.

+These authors equally contributed to this article.

#Co-lead authors.

§Correspondence to Jean-Emmanuel Sarry, Centre de Recherches en Cancérologie de Toulouse, 2 Av. Hubert Curien, 31100 Toulouse, France, Phone : 33 (0)5 62 74 45 13, E-mail : jean-emmanuel.sarry@inserm.fr and Jerome Tamburini, Faculty of Medicine, University of Geneva, rue Michel Servet 1, 1206 Geneva, Switzerland, Phone: 41 (0)22 379 52 97, E-mail : jerome.tamburinibonnefoy@unige.ch.

Running title: C/EBP α and lipid peroxidation in FLT3-driven leukemia

Key words: Ferroptosis, fatty acid biosynthesis, C/EBP α , FLT3-ITD, AML,

Disclosure of Potential Conflicts of Interest

C Récher reports receiving grant support and honoraria from Celgene, Sunesis Pharmaceuticals, Amgen, Novartis, Jazz Pharmaceuticals, Astellas Pharma, and Daiichi Sankyo and honoraria from Incyte, AbbVie, MacroGenics, and Otsuka Pharmaceutical. JE Sarry is a consultant/advisory board member for Servier. No potential conflicts of interest were disclosed by the other authors.

ABSTRACT

While transcription factor C/EBP α is critical for normal and leukemic differentiation, its role on cell and metabolic homeostasis is largely unknown in cancer. Here, multi-omics analyses uncovered a coordinated activation of C/EBP α and Fms-like tyrosine kinase 3 (FLT3) that increased lipid anabolism *in vivo* and in patients with FLT3-mutant acute myeloid leukemia (AML). Mechanistically, C/EBP α regulated FASN-SCD axis to promote fatty acid (FA) biosynthesis and desaturation. We further demonstrated that FLT3 or C/EBP α inactivation decreased mono-unsaturated FA incorporation to membrane phospholipids through SCD downregulation. Consequently, SCD inhibition enhanced susceptibility to lipid redox stress that was exploited by combining FLT3 and glutathione peroxidase 4 inhibition to trigger lipid oxidative stress, enhancing ferroptotic death of FLT3-mutant AML cells. Altogether, our study reveals a C/EBP α function in lipid homeostasis and adaptation to redox stress, and a previously unreported vulnerability of FLT3-mutant AML to ferroptosis with promising therapeutic application.

SIGNIFICANCE

FLT3 mutations are found in 30% AML cases and actionable by tyrosine kinase inhibitors (TKI). Here, we discovered that C/EBP α regulates fatty acid biosynthesis and protection from lipid redox stress downstream mutant-FLT3 signaling, which confers a vulnerability to ferroptosis upon FLT3 inhibition with therapeutic potential in AML.

INTRODUCTION

Acute myeloid leukemia (AML) are aggressive hematological malignancies characterized by an aberrant proliferation of myeloid progenitors leading to an impairment of normal hematopoiesis. *FLT3* mutations are detected in 30% of AML cases at diagnosis and are associated with adverse prognosis due to frequent relapse after intensive chemotherapy (1–4). Most *FLT3* mutations are internal tandem duplication (ITD) in the juxta-membrane domain, while tyrosine kinase domain (TKD) point mutations are less frequently detected (1). Both ITD and TKD mutations result in a constitutive activation of FLT3-dependent signaling pathways, supporting cell proliferation and survival through enhanced glucose, amino acid and redox metabolism (5–9). Recently, FLT3 inhibitors (FLT3i) such as midostaurin or gilteritinib (GILT) were shown to improve therapeutic response in *FLT3*-mutated AML patients when combined with intensive chemotherapy frontline, or used as a monotherapy in the relapse setting (10,11). However, resistance to FLT3i commonly appears, involving paracrine signaling and metabolic sensing from bone marrow microenvironment (12–17), emergence of drug-resistant secondary *FLT3* mutations or clonal escape through activation of alternative pathways, as seen with RAS-activating mutations (17–20).

C/EBP α -enhancer binding protein α (C/EBP α , encoded by the *CEBPA* gene) is a key transcription factor of myeloid differentiation (21). Different *CEBPA* mutations are detected in 5-9% of AML cases at diagnosis, with prognostic implications (1,22). Moreover, *CEBPA* expression is downregulated in AML subtypes such as those harboring *RUNX1-CBF2T1* fusion gene, which participate to differentiation block, highlighting the importance of C/EBP α in leukemogenesis (23). Beside these hematopoietic functions, C/EBP α is a critical regulator of transcriptional programs related to glucose and lipid metabolism, promoting lipogenic and gluconeogenic gene expression programs in normal adipocytes and hepatocytes (24–26). However, the role of C/EBP α in cancer and leukemic metabolism has not been studied so far.

To investigate novel metabolic dependencies of highly metabolically active mutant FLT3 AML cells (5–9), we performed multi-omics and functional approaches *in vitro*, *in vivo* using *FLT3*-mutant AML patient-derived xenograft (PDX) models, and in primary specimens from patients treated with GILT. We uncovered a novel role of C/EBP α on lipid biosynthesis downstream of FLT3. Specifically, we showed that FLT3 and C/EBP α are hierarchically activated in AML to induce the expression of Fatty Acid Synthase (*FASN*), Steroyl-CoA Desaturase (*SCD*) and Fatty Acid Desaturase 2 (*FADS2*), promoting *de novo* biosynthesis of cytoprotective mono-unsaturated fatty acids (MUFA) and generation of highly unsaturated FA from the essential poly-unsaturated FA (PUFA) linoleic acid precursor. Accordingly, inhibition of mutant FLT3 led to decreased C/EBP α and SCD expression and a relative increase in

PUFA over MUFA, impacting the distribution of cellular lipid species. This sensitized leukemic cells to lipid peroxidation and induced their vulnerability to ferroptotic cell death. Finally, we demonstrated that ferroptosis induction synergized with GILT *ex vivo* and *in vivo*, indicating new therapeutic approaches for patients with *FLT3*-mutant AML.

RESULTS

***FLT3*-mutant AML cells exhibit increased lipid biosynthesis dependent on C/EBP α**

To investigate changes in metabolic pathways of *FLT3*-activated AML cells, we analyzed differentially expressed genes (DEG) in *FLT3*-ITD-mutated MOLM-14 and MV4-11 cell lines, after *FLT3*i treatment or *FLT3* depletion by RNA interference, and we defined a *FLT3*-ITD_UP cell line signature composed of 299 downregulated genes common to these conditions compared to the control cell lines (Supplementary Fig. S1A-S1D; Supplementary Table S1). This functionally-defined signature was enriched in genes related to cell cycle and DNA/RNA processing, amino acid and redox metabolism pathways as previously described (5,27–30), and to lipid metabolism including cholesterol and fatty acid (FA) biosynthesis (Supplementary Fig. S1E; Supplementary Table S2). The same signatures were enriched in transcriptomes of *FLT3*-ITD expressing cells from a MLL-AF9-driven murine AML model (GSE1639329 (5)) (Supplementary Fig. S1F; Supplementary Table S2).

To generate *FLT3*-mutant models more relevant to patients with AML, we amplified primary leukemic cells from three different AML patients (TUH06, TUH84, TUH93) through serial transplantations in NSG mice (PDX^{TUH06}, PDX^{TUH84}, PDX^{TUH93}; Fig. 1A; Supplementary Table S3). Using this approach, we enriched samples in leukemic blasts having high variant allele frequency (VAF) of *FLT3* mutation (Fig. 1A). After *in vivo* expansion in third recipients, we performed a transcriptomic analysis on human leukemic cells incubated *ex vivo* with *FLT3*i (Fig. 1A). Using Gene Set Enrichment Analysis (GSEA), we observed a depletion of gene signatures related to glucose, amino acids, mitochondria and lipid metabolism in *FLT3*i-treated compared to control cells (Fig. 1B). Particularly, gene signatures related to lipid metabolism were strongly associated with FA and cholesterol biosynthesis, as observed in AML cell lines (Fig. 1B; Supplementary Table S4; Supplementary Fig. S1E). We further treated six *FLT3*-mutant PDXs *in vivo* with GILT after disease establishment (ie. 8-50 weeks after xenotransplantation; Fig. 1C). The genomic landscape of these samples revealed frequent concurrent *NPM1* and *DNMT3A* mutations, as expected (1) (Fig. 1D; Supplementary Table S3). Moreover, we detected *FLT3* D835Y and *NRAS* G12D mutations in TUH84 and TUH86, and TUH73 patient samples, respectively (Fig. 1D). After one week of treatment, GILT significantly reduced tumor burden in bone marrow (BM) and spleen (SP) of

four PDXs (Fig. 1E; Supplementary Fig. S2A-S2D). In PDX^{TUH86} and PDX^{TUH93}, we observed significant tumor reduction in the SP but not in the BM after 7 days GILT, while both compartments had decreased leukemia burden after two weeks treatment in PDX^{TUH93}, defining early and late responders to GILT *in vivo* (Fig. 1D and E; Supplementary Fig. S2A-S2D). Notably, the presence of *FLT3*-TKD or *NRAS* mutations was not associated with delayed GILT response in these assays (Fig. 1D and E). We performed differential gene expression analysis in human leukemic cells sorted from vehicle- and GILT-treated mice, and showed a depletion of gene signatures related to glucose, amino acids, mitochondrial and lipid metabolism in the GILT-treated conditions (Fig. 1F; Supplementary Table S5). Among lipid-related gene signatures, FA and cholesterol biosynthesis pathways were the most prominently depleted by GILT treatment *in vivo* (Fig. 1F; Supplementary Table S5).

We next aimed to identify important effectors of lipid metabolism upon FLT3 inhibition in AML. To capture these variations, we performed a quantitative proteomic analysis in FLT3i-treated MOLM-14 and MV4-11 cells. First, we observed a downregulation of Stearoyl-CoA Desaturase (SCD) involved in mono-unsaturated FA (MUFA) biosynthesis, and of Fatty Acid Desaturase 2 (FADS2) involved in the biosynthesis of highly unsaturated FA from poly-unsaturated FA (PUFA) precursors (31) (Fig. 1G; Supplementary Table S6). Importantly, we found that the protein expression of transcription factor C/EBP α and C/EBP β was decreased upon FLT3 inhibition (Fig. 1G; Supplementary Table S6), and we confirmed that FLT3i decreased the protein expression of C/EBP α by 38% in five FLT3-mutant AML PDX samples (Fig. 1H and I).

Next, we investigated the regulation of C/EBP α expression downstream of mutant FLT3 signaling. Focusing on samples having the 25% highest *CEBPA* expression in four independent cohorts of patients with AML (32–35), we observed an increased frequency of *FLT3*-ITD mutations (Supplementary Fig. S3A), but not of other signaling-related variants including *FLT3*-TKD, *NRAS* or *KRAS* mutations compared to the lower quartile (Supplementary Fig. S3A-S3C). However, we found no clear association between *FLT3*-ITD status and *CEBPA* mRNA or protein expression in the same cohorts without filtering on high *CEBPA* mRNA expression (Supplementary Fig. S3D and S3E). To investigate protein stability after FLT3i treatment in AML cells, we annotated our proteomics data with a repository of quantified protein half-lives (36), and showed that proteins downregulated after QUIZ treatment had significantly shorter half-lives compared to those increased after QUIZ (Supplementary Fig. S3F and S3G). These data suggested that QUIZ treatment induced a global inhibition of short-lived proteins.

Accordingly, we hypothesized that C/EBP α could have been subjected to a post-translational regulation downstream mutant FLT3 signaling. C/EBP α could be

phosphorylated downstream of FLT3-ITD activation (37,38). We observed that treatment with FLT3i decreased both FLT3 signaling and C/EBP α phosphorylation at Ser-21, and also reduced the amounts of C/EBP α protein in MOLM-14 and MV4-11 cells (Supplementary Fig. S4A and S4B). Next, we hypothesized that upon FLT3-ITD inhibition, unphosphorylated C/EBP α could be degraded by the ubiquitin/proteasome system. We conditionally expressed various *CEBPA* forms including untagged and tagged (HA) wild type (WT), and phosphomimetic and non phosphomimetic Ser-21 variants (S21D and S21A, respectively) in FLT3-ITD AML cell lines (Supplementary Fig. S5A and S5B). First, we observed that incubation with the proteasome inhibitor bortezomib led to the accumulation of HA-tagged C/EBP α after induction by doxycycline (dox; Supplementary Fig. S5C). Similarly, proteasome inhibition induced a significant and near-significant accumulation of WT or S21D forms, respectively, but had no impact on the expression of the S21A non phosphomimetic variant of *CEBPA* (Supplementary Fig. S5D and S5E). This indicates that Ser-21 phosphorylation contributed to post-translational regulation of C/EBP α expression in AML.

In FLT3-mutated PDX samples, we also confirmed that FLT3i decreased the expression of *SCD* and *FADS2*, as well as of Sterol Regulatory Element-Binding Protein 1 (SREBP1) protein expression, which is a transcription factors involved in FA biosynthesis (39) (Fig. 1H and I). In contrast, FLT3i decreased the mature form of SREBP1 but not of SREBP2 (known to be involved in cholesterol biosynthesis) in leukemic cell lines (Supplementary Fig. S6A and S6B). This highlights that FLT3 inhibition predominantly redirected lipid metabolism towards FA biosynthesis rather than cholesterol biosynthesis inhibition. Interestingly, FLT3i decreased the mRNA expression of *SCD*, *FASN* and *FADS2* but not the mRNA expression of *CEBPA* in primary AML samples and AML cell lines (Supplementary Fig. S7A and S7B). Furthermore, *CEBPA*-OE resulted in a significant increase in these mRNA during GILT treatment compared to the empty vector (Supplementary Fig. S7C). The expression of *SCD*, *FASN* and *FADS2* was also increased in MOLM-14 cells expressing Ser-21 mutant compared to WT *CEBPA* forms (Supplementary Fig. S7D). Together, these results suggested that C/EBP α transcriptionally regulated the expression of FA biosynthesis regulators downstream of FLT3-ITD in AML.

To gain insight into the mechanisms whereby C/EBP α regulates lipid metabolism, we first analyzed public databases of C/EBP α chromatin immunoprecipitation (ChIP) sequencing and observed that C/EBP α more frequently occupied the promoter regions of *SCD*, *FASN*, *SREBF1* and *DHCR24* compared to randomly chosen genes (Supplementary Fig. S8A). Next, we generated various interfering RNA approaches to achieve C/EBP α depletion within the same range as observed after FLT3i treatment in terms of protein suppression and functional activity (Supplementary Fig. S8B-S8D). We performed and combined a bulk

RNAseq and an Assay for Transposase-Accessible Chromatin sequencing (ATACseq) after C/EBP α suppression by constitutive shRNA construct to compare genome accessibility based on C/EBP α expression in MOLM14 AML cells. We identified 31,707 peaks that were differentially accessible between shCTL and shC/EBP α MOLM14 FLT3-ITD AML cells (Bedtools intersect; Fig. 1J; Supplementary Table S7). We observed that C/EBP α depletion impacted the chromatin accessibility within 10,860 genes which include lipogenic genes such *SCD*, *FASN*, *FADS2* that are downregulated by C/EBP α invalidation and QUIZ treatment (Fig. 1K-L; Supplementary Fig. S8E; Supplementary Table S7 and S8). As an example, several regions of open chromatin were identified in closed proximity to the *SCD* locus in cells expressing C/EBP α while absent or decreased in shC/EBP α cells, thus confirming the role of C/EBP α on the regulation of *SCD* gene accessibility (Fig. 1M). These results established that C/EBP α expression confers a unique chromatin accessibility landscape to FLT3-ITD AML cells.

Collectively, this indicates that mutant FLT3 signaling sustains lipid metabolism through the key FA biosynthesis effector C/EBP α .

Activation of the FLT3-C/EBP α axis is associated with lipid biosynthetic pathways

To study C/EBP α function in *FLT3*-mutant AML cells, we performed DEG analysis in MOLM-14 cells depleted in sh*CEBPA* or overexpressing (OE) C/EBP α (*CEBPA*-OE) compared to their respective control (CTL) cells. We identified 198 significantly up- and down-regulated genes after C/EBP α overexpression and depletion, respectively (Fig. 2A; Supplementary Table S9). This *CEBPA*_UP signature was enriched in genes related to cell cycle, as well as glucose, FA and cholesterol metabolism (Fig. 2B). Interestingly, we observed an enrichment of this *CEBPA*_UP signature in control compared to FLT3i-treated AML cell lines and primary AML cells, and in publicly accessible gene expression databases of *FLT3*-mutant compared to non-mutant AML cells (Fig. 2C, Supplementary Fig. S9A). Finally, we identified six genes in common between *CEBPA*_UP and *FLT3*-related gene signatures, and among them, four encoded key enzymes involved in FA (*SCD* and *FASN*) or cholesterol (*DHCR7* and *DHCR24*) biosynthesis (Fig. 2D; Supplementary Table S10).

Next, we investigated intra-tumor transcriptional heterogeneity and response to FLT3i *in vivo* using single cell RNA sequencing (scRNA-seq) on sorted human AML cells from vehicle- and GILT-treated mice of three FLT3-ITD PDX models (Fig. 2E). From bulk DNA sequencing in two of these PDXs, we observed that FLT3-ITD allele VAF were 46% and 81% in PDX^{TUH93} and PDX^{TUH110}, respectively. This indicates that a majority of leukemic cells analyzed by scRNAseq after *in vivo* exposure to GILT harbored a FLT3-ITD mutation

(Supplementary Fig. S9B and S9C). Using Seurat and unsupervised hierarchical clustering analysis on each cell transcriptomes, we uncovered distinct clusters defined by their transcriptional state (PDX^{TUH93}, Fig. 2F). The presence and proportion of cells in these states fluctuated between vehicle- and GILT-treated mice (Fig. 2G and H). First, we observed an enrichment of the FLT3-ITD_UP cell line signature in GILT-sensitive clusters from the vehicle conditions, highlighting the cells harboring an activation of FLT3-ITD (cluster #8 for PDX^{TUH93}, Fig. 2H and I, and Supplementary Fig. S9D). This was associated with a concomitant enrichment of CEBPA_UP signature in the GILT-sensitive clusters in the vehicle conditions (Fig. 2J and Supplementary Fig. S9E). Interestingly, *SCD*, *FASN* and *FADS2* were co-expressed and enriched in cells with an activation of FLT3-ITD in vehicle groups, and this cluster of co-expression was depleted upon GILT treatment (Fig. 2K). When independently applied to all PDXs, this consensus *SCD* co-expressed cluster was enriched in cells harboring an activation of both FLT3-ITD and CEBPA_UP signatures in vehicle groups (Fig. 2K and L, and Supplementary Fig. S9F). Notably, enrichment in both FLT3-ITD_UP cell line and CEBPA_UP signatures was not restricted to cells harboring a high expression of *MKI67* gene related to cell cycle (Supplementary Fig. S9G and S9H). Similar results were observed for PDX^{TUH84} (cluster #2) and PDH^{TUH110} (cluster #3) (Supplementary Fig. S10A-L and S11A-L).

Together, these transcriptional analyses showed the regulation of lipogenic gene expression by the FLT3-C/EBP α axis in *FLT3*-mutant leukemic cells.

C/EBP α regulates rate-limiting lipid biosynthetic enzymes downstream of FLT3-ITD

We next investigated the role of C/EBP α in the anti-leukemic activity of FLT3i towards FLT3-mutant cells. First, we analyzed the transcriptomes of primary blasts from 21 patients with AML collected before (n=20) and/or during (n=17) GILT therapy (median duration: 54 [27-589] days) which include 16 paired pre-/post-GILT specimens (Fig. 3A; Supplementary Table S11). We observed a significant correlation between the CEBPA_UP signature and FLT3-ITD_UP signature and *MKI67* expression across these samples (Supplementary Fig. S12A; Supplementary Table S12). Next, we stratified patient response based on the enrichment (AML patient group 1) versus the depletion (AML patient group 2) of CEBPA_UP signature after GILT treatment (Fig. 3A). We showed that FLT3-ITD-related signatures and *MKI67* gene expression were up-regulated in group 1 (Fig. 3B and 3C) and not modified in group 2 (Supplementary Fig. S12B and S12C). We further observed that all group 1 patients and the majority of group 2 patients displayed a low or high enrichment in the CEBPA_UP signature before GILT, respectively (Supplementary Fig. S12D). Interestingly, when focusing on group 1 patients, GSEA revealed an enrichment in FLT3-related signatures from

independent studies (8,40), alongside with *MKI67* and *CEBPA_UP* signatures after clinical failure of GILT (Supplemental Fig. S12E). These results suggested that *CEBPA* could be associated with clinical resistance to GILT in a subset of patients with *FLT3*-ITD AML.

Using doxycycline (dox)-inducible shRNAs, we achieved a partial inhibition of C/EBP α expression in MOLM-14 cells (Fig. 3D; Supplementary Fig. S13A). Interestingly, the expression of enzymes involved into lipid metabolism including SCD, FASN and FADS2 decreased upon C/EBP α depletion (Fig. 3D; Supplementary Fig. S13A). In *FLT3*-ITD AML cell lines, C/EBP α depletion significantly reduced the sensitivity threshold to FLT3i (Fig. 3E; Supplementary Fig. S13B). Moreover, in three independent MOLM-14 cell line-derived xenograft (CLDX) assays, we observed that C/EBP α suppression significantly decreased leukemia burden and attenuated the surface expression of the differentiation markers CD14 and CD15 (Supplementary Fig. S13C-S13E) and markedly enhanced anti-AML efficacy of GILT *in vivo* (Fig. 3F and G). Finally, we harvested post-GILT residual disease from the PDX^{TUH110} model and we transfected these cells with CTL or anti-CEBPA siRNAs *ex vivo* to perform a secondary transplantation in NSG mice (Supplementary Fig. S13F). We observed that CEBPA suppression induced a 3-fold decrease in the propagation of leukemic cells into secondary recipient mice (Supplementary Fig. S13G). These results showed that C/EBP α participated to survival pathways downstream of FLT3-mutant signaling in AML.

Next, we observed that *CEBPA*-OE significantly induced SCD, FASN and FADS2 expression in MOLM-14 cells, which was decreased after incubation of AML cells with FLT3i (Fig. 3H; Supplementary Fig. S13H). Notably, the cytotoxicity of FLT3i was significantly alleviated in *FLT3*-ITD AML cells overexpressing C/EBP α (Fig. 3I and J; Supplementary Fig. S13I). When transplanted into NSG mice, *CEBPA*-OE MOLM-14 cells showed a slight decrease in engraftment capacities, and an increase in the expression of the differentiation markers CD14 and CD15 compared to the empty vector control (Fig. 3K). Finally, we overexpressed WT, S21A or S21D *CEBPA* forms in MOLM-14 cells, and while the three isoforms significantly protected AML cells from FLT3i treatment, this effect was more marked in S21D-expressing AML cells (Fig. 3L; Supplementary Fig. S13J), suggesting that the inhibition of Ser-21 phosphorylation upon FLT3i impaired the pro-survival function of C/EBP α .

Collectively, these results highlight that C/EBP α through, at least in part, the regulation of lipid biosynthetic enzymes favors AML cell survival downstream of mutant FLT3 signaling pathway.

C/EBP α drives fatty acid biosynthetic fluxes in *FLT3*-mutant leukemic cells

To characterize lipid metabolism in *FLT3*-mutant AML, we performed global lipidomic analyses in MOLM-14 and MV4-11 cells treated with FLT3i. We observed a global decrease in glycerophospholipid (GPs) categories, including phosphatidylethanolamines (PEs) and phosphatidylcholines (PCs), and an increased triglycerides (TGs) content after FLT3i (Supplementary Fig. S14A; Supplementary Table S13). To evaluate if these lipid metabolic changes were driven by C/EBP α , we performed global lipidomic analyses in C/EBP α -depleted or in C/EBP α -OE MOLM-14 cells treated with FLT3 inhibitor quizartinib (QUIZ) or vehicle. While C/EBP α suppression recapitulated the lipidomic profile observed upon FLT3i, C/EBP α -OE showed the opposite with increased PEs, PCs and their derivatives (lyso-PCs (LPCs), lyso-PEs (LPEs)), and decreased TGs content, and strikingly this lipid distribution was abolished upon FLT3i (Fig. 4A; Supplementary Fig. S14B-S14H; Supplementary Table S13). As lipid droplets represent a reservoir for intracellular TG, we also performed electron microscopy, and we observed that FLT3 inhibition led to increased number of lipid droplets in *FLT3*-mutant AML cell lines (Supplementary Fig. S15A and B). Similarly, C/EBP α depletion increased cellular neutral lipid content in MOLM-14 cells (Supplementary Fig. S15C). However, we observed a decreased expression of TG carriers including FABP5, SLC27A4 and SLC27A2, and an increase in FA transporters such as CD36 or SLC27A3 in leukemic cells after FLT3 or C/EBP α inhibition (Supplementary Fig. S15D). Accordingly, FLT3 or C/EBP α inhibition led to decreased lipid import through the plasma membrane in *FLT3*-mutant patient-derived cells and cell lines (Supplementary Fig. S15E). Finally, the sphingolipids ceramides (CER) and sphingomyelins (SM) were increased in *FLT3*-mutant cell lines after FLT3 or C/EBP α inhibition (Fig. 4A; Supplementary Fig. S14A-S14H). These results showed distinct regulation of glycerophospholipid and neutral lipids by the FLT3-ITD-C/EBP α axis in *FLT3*-mutant AML cells.

To follow the contribution of glucose and glutamine into FLT3-ITD-dependent FA synthesis, we performed untargeted lipidomic analysis using liquid chromatography coupled with high-resolution mass spectrometry (LC-HRMS) of MOLM-14 and MV4-11 incubated with FLT3i, and grown with stable uniformly labeled isotopologues of $^{13}\text{C}_6$ -glucose ($^{13}\text{C}_6$ -Glc) or $^{13}\text{C}_5$ -glutamine ($^{13}\text{C}_5$ -Gln) (Fig. 4B). In this setting, incubation with FLT3i slightly decreased cell viability and density (Supplementary Fig. S16A). Moreover, the mean normalized enrichment of both $^{13}\text{C}_6$ -Glc and $^{13}\text{C}_5$ -Gln into newly synthesized FA was significantly decreased after FLT3i treatment (Fig. 4C; Supplementary Fig. S16B). Notably, isotopologue distribution showed a marked reduction of isotopes incorporation from 14:0 species, suggesting that fluxes of both glucose and glutamine oxidation to support MUFA biosynthesis were reduced upon FLT3 inhibition in *FLT3*-mutant leukemic cells (Fig. 4D; Supplementary Fig. S16C).

Collectively, targeted and isotope tracing lipidomics revealed that FLT3 regulated FA biosynthetic activities in *FLT3*-mutant AML cells in a C/EBP α -dependent manner.

FLT3 inhibition decreases mono-unsaturated fatty acids dependent on C/EBP α

Fatty acid biosynthesis mostly provides SFAs and MUFAs, while PUFAs are available mostly by food intake and subjected to both desaturation and elongation through FADS and ELOVL, respectively (31,41) (Fig. 5A). SFAs and PUFAs are cytotoxic and can be stored into lipid droplets (41). Particularly, PUFAs form lipid complexes with reactive oxygen species (ROS), leading to lipid peroxidation products that trigger cell death (42) (Fig. 5A). We hypothesized that inhibition of the FLT3-C/EBP α axis could induce changes in lipid metabolism that modify the membrane phospholipid distribution of SFA:MUFA:PUFA in *FLT3*-mutant AML cells (Fig. 5A). In lipidomic profiling experiments, we first observed a decreased incorporation of both SFAs and MUFAs into phospholipids, especially PC and PE after FLT3i or C/EBP α invalidation, along with an increase in PUFA levels (Fig. 5B and C; Supplementary Fig. S17A-S17E; Supplementary Table S14). On the contrary, C/EBP α -OE increased both SFAs and MUFAs into phospholipids which was abolished by FLT3i (Fig. 5B and C; Supplementary Fig. S17A-S17E; Supplementary Table S14). Accordingly, the PUFA:MUFA ratio in phospholipids was increased after FLT3 or C/EBP α inhibition, and decreased after C/EBP α -OE in MOLM14 cells (Fig. 5D; Supplementary Fig. S18; Supplementary Table S15).

These results indicate that C/EBP α is essential to preserve lipid homeostasis through the generation of MUFAs and the control of PUFAs import and storage in *FLT3*-mutant AML cells.

Inhibition of SCD-dependent mono-unsaturated FA biosynthesis sensitizes FLT3i-treated AML cells to ferroptotic cell death

As we showed that FLT3 inhibition increased cytotoxic PUFA and decreased protective MUFA, we next investigated whether this elevation of the PUFA/MUFA ratio that promotes membrane lipid peroxidation (43) could contribute to AML cell death upon FLT3 inhibition. We thus experimentally manipulated the PUFA/MUFA ratio *via* SCD inhibition or overexpression, glutathione peroxidase (GPX4) inhibition, since this anti-oxidant enzyme specifically catalyzes the reduction of lipid peroxides using reduced glutathione (GSH) (44), or direct MUFA (oleate) supply. We hypothesized that the PUFA/MUFA ratio will mechanistically links mutant FLT3 signaling and ferroptosis, a non-apoptotic form of cell death triggered by lipid peroxidation (42) (Fig. 6A; Supplementary Fig. S19A).

In MOLM-14 and MV4-11 AML cell lines, the GPX4 inhibitor RSL3 (44) had anti-leukemic activity with IC₅₀ values of 86 nM and 106.7 nM, respectively, which was fully rescued by the synthetic anti-oxidant ferrostatin-1 (Fer-1; Supplementary Fig. S19B). As the dose-response curves of RSL3 were close to an “on/off” pattern, we arbitrarily defined non-cytotoxic (100 nM) and cytotoxic (250-500 nM) RSL3 concentrations when we aimed to enhance or to attenuate the effects of RSL3 in AML cells, respectively. Next, we incubated MOLM-14 and MV4-11 cells with RSL3, and a MUFA (oleate) or vehicle (bovine serum albumin), and observed that oleate significantly rescued their viability, which correlated with reduced lipid oxidation in MOLM-14 and MV4-11 cells (Fig. 6B and C; Supplementary Fig. S19C). These results showed that ferroptotic cell death was actionable through GPX4 inhibition in FLT3-ITD AML cells.

To assess the specific role of mutant FLT3 signaling on lipid peroxidation (lipid-ROS), we used the Ba/F3 murine hematopoietic cell line constitutively expressing *FLT3*-ITD (Ba/F3-ITD, growth factor independent), which display exclusive addiction to *FLT3*-ITD signaling (45,46), or non-mutated *FLT3* allele (Ba/F3-WT, dependent on FLT3 ligand). We observed that RSL3 induced lipid-ROS formation in Ba/F3-ITD cells but not in Ba/F3-WT cells, which was markedly enhanced by co-incubation with QUIZ, and attenuated by oleate supply (Supplementary Fig. S19D). In the same vein, we forced endogenous MUFA production by overexpressing SCD (SCD-OE), the rate-limiting enzyme of the last step of MUFA biosynthesis, in MOLM-14 and MV4-11 cell lines. We observed that SCD-OE significantly protected AML cells from FLT3i (Fig. 6D and E). This provided a functional validation that SCD acted as downstream of FLT3-mutant signaling. Accordingly, we showed that SCD-OE markedly protected leukemic cells from lipid peroxidation and cell death induced by cytotoxic concentrations of RSL3 (Fig. 6F-H).

Finally, the depletion of SCD by two distinct lentivirally-transduced shRNAs (Fig. 6I) markedly enhanced lipid peroxidation and cell death in *FLT3*-mutant AML cells when incubated with non-cytotoxic concentrations of RSL3, as compared to their shCTL counterpart (Fig. 6J and K). Then, we used a small molecule SCD inhibitor (MF-438; (47)), which demonstrated a moderate anti-leukemic activity as single agent, and a synergistic effect when combined with FLT3i against *FLT3*-mutant AML cell lines and primary patient samples (Fig. 6L). In line with the effects of SCD depletion, lipid-ROS generation and cell death induced by non-cytotoxic concentrations of RSL3 were markedly amplified by co-incubation with MF-438 (Supplementary Fig. S19E and S19F).

These results showed that the relative PUFA/MUFA content determines the susceptibility of AML cells to ferroptotic cell death, which could represent a new vulnerability of *FLT3*-ITD leukemic cells.

FLT3 inhibition primes *FLT3*-mutant leukemic cells to ferroptotic cell death

We therefore wondered whether alterations in cellular lipid homeostasis induced by acute inhibition of mutant FLT3 signaling increased susceptibility to ferroptotic cell death, which could be exploited to define new therapeutic strategies for patients with AML. In *FLT3*-mutant cell lines, cell death observed after C/EBP α depletion was increased by RSL3, while C/EBP α overexpression partly protected leukemic cells from GPX4 inhibition (Fig. 7A). Moreover, while FLT3i or shFLT3 had a modest effect on lipid peroxidation, their combination with RSL3 markedly enhanced lipid peroxidation and cell death in *FLT3*-ITD cell lines (Fig. 7B and C; Supplementary Fig. S20A and S20B). Interestingly, Ba/F3-ITD cells had a limited sensitivity to RSL3 alone, but the incubation with QUIZ significantly sensitized Ba/F3-ITD cells but not Ba/F3-WT cells to RSL3 (Supplementary Fig. S20C). Next, we also observed a synergy between QUIZ and RSL3 in patient-derived AML cells *ex vivo*, and in MOLM-14 and MV4-11 cell lines (Fig. 7D; Supplementary Fig. S20D). Notably, we confirmed that FLT3 inhibitor GILT increased lipid-ROS by 2.5-fold *in vivo* as assessed by anti-4-hydroxynonenal (4-HNE) staining in bone marrow from three PDX models (Supplementary Fig. S20E). We observed that three other FLT3 inhibitors (crenolanib, midostaurin and sorafenib) enhanced the vulnerability of MOLM-14 and MV4-11 cells to RSL3, and that this effect was fully reverted by co-incubation with Fer-1 (Supplementary Fig. S20F). On the other hand, the vulnerability to FLT3i was enhanced by two other GPX4 inhibitors FIN56 and ML210 that was abrogated by Fer-1 (Supplementary Fig. S20G and S20H). Finally, the SLC7A11 inhibitor erastin that targets the antioxidant GSH thereby promoting ferroptosis (48), also synergized MOLM14, MV4-11, Ba/F3-ITD or UT-7-ITD (but not Ba/F3-WT or UT-7-WT) cells to QUIZ treatment *in vitro* (Supplementary Fig. S20I). These results showed that FLT3 inhibition primed leukemic cells with mutant FLT3 oncogenic addiction to lipid oxidation and ferroptotic cell death.

We next investigated the cooperative lethality between redox stress induction and FLT3 inhibition *in vivo*. We depleted *GPX4* by CRISPR/Cas9 in MOLM-14 cells (Supplementary Fig. S21A). As *GPX4* knockout (KO) is lethal in our model, AML cells were grown *in vitro* with Fer-1 that efficiently prevented lipid oxidation and cell death in *GPX4*^{KO}, while Fer-1 removal promptly resulted in the opposed effect (Fig. 7E). Using a different approach by RNA interference, we similarly observed that *GPX4* depletion induced leukemic cell death, which was further enhanced by FLT3i treatment (Supplementary Fig. S21B and S21C). We then performed CLDX assays using *GPX4*^{KO} or *GPX4*^{WT} (transduced with control CRISPR) MOLM-14 cells xenografted in immunodeficient NSG mice. To allow the engraftment of viable *GPX4*^{KO} AML cells, both *GPX4*^{WT} and *GPX4*^{KO} mice were treated with Fer-1 from the

day of transplantation (Fig. 7F). After ten days, Fer-1 was stopped at a stage of established disease, and mice were treated by GILT or vehicle for one week before the assessment of leukemia burden, or followed-up for survival without further treatment (Fig. 7F). We first observed an increased BM staining with anti-4-HNE in GPX4^{KO} mice, which was re-inforced after GILT treatment (Fig. 7G). Moreover, human engraftment and total cell tumor burden were significantly reduced in GILT-treated GPX4^{WT} mice and in vehicle-treated GPX4^{KO} mice, but residual disease was nearly eradicated in GPX4^{KO} mice treated with GILT (Fig. 7H and I). This marked tumor reduction was associated with an increased survival of GPX4^{KO} mice treated with GILT (Fig. 7J). Together, these results show that lipid redox stress induction primed *FLT3*-ITD AML cells to FLT3i *in vitro* and *in vivo*.

Finally, we and others previously showed that APR-246, a promising therapeutic agent in AML (49), induces AML cell killing (50,51) by decreasing glutathione salvage and increasing lipid peroxidation (52–54). Using dose-response matrices, we observed a synergy between APR-246 and FLT3i on primary AML cells from three patients *ex vivo* (Supplementary Fig. S21D). Notably, APR-246 was also synergistic with other FLT3i including QUIZ, midostaurin and crenolanib *in vitro*, and enhanced lipid oxidation and cytotoxicity induced by shRNA-mediated FLT3 depletion in *FLT3*-ITD cell lines (Supplementary Fig. S21E-S21G). Next, we treated two established *FLT3*-ITD AML PDXs (PDX^{TUH84} and PDX^{TUH06}), and MOLM-14 CLDX with GILT and/or APR-246 during one week (Supplementary Fig. S22A). APR-246 showed moderate activity alone, and a trend to enhanced activity of GILT in MOLM-14 CLDX experiments (Supplementary Fig. S22B). In PDX assays, we observed no significant APR-246 single-agent activity, but a significant increase in GILT effect by APR-246 in one PDX, which correlated to an increased lipid-ROS content (PDX^{TUH84}, Supplementary Fig. S22C-S22E). Notably, no toxicity was observed with APR-246 as assessed by quantification of murine hematopoietic cells and body weight (Supplementary Fig. S22F-S22H). Interestingly, APR-246 significantly decreased tumor growth in chick chorio-allantoic membrane (CAM)-based assays developed as an alternative MOLM-14 xenograft model, and this effect was moderately enhanced by co-incubation with GILT (Supplementary Fig. S22H-S22J).

Collectively, these preclinical experiments uncover a sensitivity of *FLT3* mutant AML cells to ferroptosis inducers that is unmasked by acute *FLT3* inhibition in a CEBPa-SCD dependent manner, suggesting that this synthetic lethality could be exploited in future therapeutic strategies for patients with *FLT3*-mutant AML.

DISCUSSION

FLT3 is the most frequently mutated gene in AML, leading to an overactivation of signaling pathways downstream this tyrosine kinase receptor. This results in a high proliferation rate of leukemic cells and frequent relapse after intensive chemotherapy. The practice-changing approval of FLT3i at different stages (first line, relapse and post-allogenic stem cell transplant maintenance) of AML therapy provides a significant survival gain for patients with AML (10,11,55). However, resistance to FLT3i is common and caused by multiple mechanisms including selection of FLT3i-resistant clones harboring *FLT3*-TKD or RAS-activating mutations, or signaling or metabolic adaptations to FLT3i (19,56,57). The discovery of novel vulnerabilities is therefore an important goal in *FLT3*-mutant AML to uncover alternative therapeutic strategies targeting post-FLT3i residual disease and preventing the emergence of resistance.

In this study, we demonstrated that the biosynthesis of lipids (including FA, glycerophospholipids, sphingolipids and triglycerides) is a critical vulnerability and dependency of *FLT3*-mutant AML mediated by the transcription factor C/EBP α . Amongst metabolic adaptations (5,8), AML cells with *FLT3*-ITD mutations display activated FA oxidation and increased lysophospholipid amount (58). Moreover, ceramides (a type of sphingolipids) are involved in cell cycle arrest and apoptotic cell death in cancer models (59) and *FLT3*-ITD represses their biosynthesis in leukemia (60), suggesting that ceramide accumulation as observed in our lipidomic assays might contribute to leukemic cell death mediated by FLT3i. Furthermore, AML cell death induced by ceramide might be regulated by GPX4 activity, as previously described with the isoenzyme GPX1 (61), suggesting that intricate cell death modalities including apoptosis and ferroptosis could be triggered upon acute FLT3 inhibition dependent on impairment in lipid metabolism of mutant FLT3 AML cells. Interestingly, high-fat diet promotes FLT3-dependent leukemia in MLL-AF9 AML mouse model, highlighting a crucial role of lipid homeostasis with this oncogene (62). Interestingly, lipid dependency is not restricted to FLT3-mutant AML and is also observed in leukemia with other drivers such as oncogenic isocitrate dehydrogenase isoforms, which can redirect lipid metabolism towards FA oxidation to maintain mitochondrial oxidative phosphorylation by activating C/EBP α -driven transcriptional program (63). Using a multi-omics approach *in vitro* and *in vivo*, we showed that C/EBP α is a novel essential regulator of FA biosynthesis through the activation of SCD, a rate-limiting enzyme for MUFA biosynthesis (64), downstream *FLT3*-mutant receptors. This lipid dependency of *FLT3*-mutant AML was further observed at the single cell level *in vivo* in PDX assays, highlighting the link between SCD, lipid peroxidation, ferroptosis priming and post-FLT3i residual disease *in vivo*. In same vein, acyl-CoA dehydrogenase involved into FA metabolism protects glioblastoma cells from toxic lipid oxidation, which favors their adaptive resistance to drug-induced stress (65,66).

Together, C/EBP α may account for the high reliance of leukemic cells on sustained FA catabolic (63) or anabolic (this present study) pathways.

Isotope tracing lipidomic experiments uncovered that FLT3 inhibition strongly reduced glucose and glutamine utilization to fuel FA biosynthesis, and that C/EBP α inhibition resulted in the same shift in lipid composition with decreased and increased amounts of phospholipids and neutral lipids, respectively. Based on our previous study (67), this accumulation of neutral lipids might be due to autophagy/lipophagy inhibition. Among lipid species, FLT3 and C/EBP α inhibition particularly reduced the amounts of MUFA through SCD inhibition alongside with increased PUFA import and storage as compensatory adaptation to FADS2 inhibition. Because imported PUFA are more susceptible to peroxidation, lipogenesis inhibitors increase the levels of peroxidation end products, render cancer cells more susceptible to oxidative stress-induced cell death, and act as chemotherapeutic sensitizers (68). Interestingly, periodic fasting-mimicking and calorie-restriction diets inhibit SCD, decrease MUFA, alter MUFA:SFA ratio and affect tumor growth in mice (69,70). Our study also showed that an increase in both PUFA:MUFA ratio and propensity to lipid oxidation as achieved by inhibition of the FLT3-C/EBP α -SCD axis represents a window of opportunity to trigger ferroptotic cell death (66). Accordingly, targeting the critical regulator of redox/ROS homeostasis GPX4 was synergistic with FLT3, C/EBP α or SCD inhibition in FLT3-mutant AML cells.

Ferroptosis recently emerged as an iron-dependent, non-apoptotic form of regulated cell death particularly relevant to cancer therapy, with implications in response to chemotherapy, radiotherapy and immunotherapy (71–73). While we showed the potential of ferroptosis induction in FLT3-ITD AML *in vivo* using a genetic model of GPX4 suppression, currently available direct GPX4 inhibitors such as RSL3 showed limited selectivity and pharmacokinetic properties *in vivo* (74). In contrast, indirect GPX4 inhibition that might be achieved by inhibition of cyst(e)in/selenocystein import through SLC7A11 or LRP8 blockage, could represent a promising approach to therapeutic ferroptosis induction in patients with cancer (53,75). We also recently showed that the small molecule APR-246 strongly induces ferroptosis through GSH depletion (53). Interestingly, APR-246 is now known as eprentapopt and was successfully administered to patients with myeloid neoplasms including AML in phase II clinical trials in association with azacitidine (49,76). We therefore used APR-246 to trigger lipid oxidation in AML cells, and observed a synergy between APR-246 and diverse FLT3 inhibitors including gilteritinib, quizartinib, midostaurin and crenolanib, compared to single agents *in vitro*. Moreover, APR-246 also enhanced GILT activity *in vivo* in FLT3-mutant AML PDX models. This further uncovered lipid oxidation as a new target in FLT3-mutant AML.

In summary, we describe a novel and protective role of C/EBP α from ferroptotic cell death in cancer through the transcriptional control of SCD-driven MUFA biosynthesis. Similar role of SCD was observed in cancer and ferroptosis (77). Our study also demonstrates that FLT3 inhibition causes metabolic changes in response to C/EBP α -SCD downregulation that induce lipid oxidation and therefore leukemia cell death, which is therapeutically actionable by ferroptosis inducers in AML cells (Fig. 7K).

METHODS

Samples from patients with AML

De-identified frozen primary specimens from patients with AML are from Toulouse University Hospital (TUH) (Toulouse, France), Lyon University Hospital (Lyon, France), Barts Cancer Institute, Queen Mary University of London (London, United Kingdom), Peter MacCallum Cancer Centre, Royal Melbourne Hospital (Melbourne, Australia) and Perelman School of Medicine, University of Pennsylvania (Philadelphia, PA, USA). A signed written informed consent for research use was obtained for each patient in accordance with the Declaration of Helsinki. Biobank collections are established according to the specific laws of each country, and transfer agreement for research applications were obtained after approbation by institutional review boards and ethics committees. Patient characteristics are summarized in Supplementary Table S3 and S11. The cytogenetic and genomic landscape of these leukemia samples was obtained during routine diagnosis procedures. Samples from TUH were processed for large-scale genomic analysis using AmpliSeq for Illumina Myeloid Panel (Illumina, San Diego, USA), and *FLT3*-ITD mutations were also investigated by quantitative and fluorescent PCR (Eurofins Genomics, Luxembourg), allowing the calculation of a ratio between ITD and wild type *FLT3* alleles.

AML cell lines

MOLM-14 and MV4-11 human AML cell lines are STR (short tandem repeat, PCR-single-locus-technology, Promega PowerPlex21 PCR Kit, Eurofins Genomics) profiled periodically, and verified mycoplasma negative yearly. MOLM-14 harbors a heterozygous *FLT3*-ITD mutation while MV4-11 carries a homozygous *FLT3*-ITD mutation (78). AML cell lines were maintained at low passage number (8-10) in RPMI L-Glutamine (4 mM) supplemented or minimum essential medium (MEM)- α Glutamax supplemented with 10% foetal bovine serum (FBS, Invitrogen), 100 IU/mL penicillin and 100 μ g/mL streptomycin (Life Technology) at 37°C with 5% CO₂, and split every 2–3 days before reaching confluence. After being thawed

from STR-authenticated batch, AML cell lines were passaged a maximum of 5 times (2 weeks) prior to use in experiments.

Reagents

Doxycycline (Sigma-Aldrich, Cat# D9891) was used at 1 µg/mL. RSL3 (Cat# HY-100218A), MF-438 (Cat# HY-15822), Ferrostatin-1 (Fer-1, Cat# HY-100579), Gilteritinib (GILT, Cat# HY-12432) and Quizartinib (QUIZ, Cat# HY-13001) were all from MedChemExpress. Oleate (Oleic Acid-Albumin from BSA, Cat# O3008) was from Sigma-Aldrich.

AML mouse xenograft model

Animals were used in accordance with a protocol reviewed and approved by the Institutional Animal Care and Use Committee of Region Midi-Pyrenees (France). NOD/LtSz-SCID/IL-2R γ chain null (NSG) mice were produced at the Genotoul Anexplo platform in Toulouse, France, using breeders obtained from Charles River Laboratories. Mice (6–9 weeks old) were treated with busulfan (20 mg/kg for MOLM-14 and 30 mg/kg for PDXs) 24 h before injection of leukemic cells. Leukemia samples were thawed at room temperature, washed twice in PBS1X, and suspended in Hank's Balanced Salt Solution (HBSS) at a final concentration of 0.2-10 \times 10⁶ cells for PDXs and 1 \times 10⁶ for cell line-derived xenograft (CLDX) per 200 µl of HBSS per mouse for tail vein injection. *PDX models*: After engraftment (defined as >20/µL human leukemic cells in peripheral blood), mice were randomly assigned to the different treatment arms. PDXs were treated with vehicle or GILT after engraftment of human leukemic cells (8–18 weeks after AML cells transplantation). GILT was solubilized in water containing 0.5% methylcellulose 400cp (Sigma-Aldrich, Cat# M0262), mice were treated daily for 7 days or 14 days by oral gavage with 30 mg per kg (mpk) GILT. *CLDX models*: MOLM-14 cells transduced with control or *GPX4*-targeting CRISPR-Cas9 guides were transplanted to NSG mice, which were treated from the day before transplant by intraperitoneal injection of 2 mpk Fer-1 during 10 days. Next, mice were treated by daily oral gavage with 10 mpk GILT or vehicle during 7 days.

Assessment of human AML engraftment

NSG mice were euthanized in accordance with European ethics protocols. Bone marrow from tibias, femurs and hips, and spleen were dissected and flushed in HBSS with 1% FBS. Mononuclear cells from bone marrow and spleen were labeled with mCD45.1-PerCP-Cy5.5 (Cat# 560580, RRID: AB_1727489), hCD45-APC (Cat# 555485, RRID:AB_398600) and hCD44-PECy7 (Cat# 560533, RRID:AB_1727483) or hCD33-PE (Cat# 555450, RRID:AB_395843; all antibodies from BD Biosciences), and Annexin V-V500 (BD Biosciences Cat# 561501, RRID:AB_10694254) to determine the fraction of viable human

blasts (AnxV-hCD45+mCD45.1-hCD44+ or AnnxVhCD45+mCD45.1-hCD33+ cells) using flow cytometry. Analyses were performed on a CytoFLEX flow cytometer with CytExpert software (Beckman Coulter, RRID:SCR_017217) and FlowJo 10.2 (Tree Star, RRID:SCR_008520). The number of AML cells/ μ l peripheral blood and number of AML cells in total cell tumor burden (in bone marrow and spleen) were determined by using CountBright beads (Invitrogen) using described manufacturer protocol.

Flow cytometry cell sorting

Human AML cells harvested from AML-xenografted mice were stained with Fixable Viability Stain 510 (BD Biosciences Cat# 564406, RRID:AB_2869572) and the following fluorescent conjugated antibodies: hCD45-APCH7 (Cat# 641399, RRID:AB_1645735) and hCD33-PE (Cat# 555450, RRID:AB_395843; all antibodies from BD Biosciences) by BD FACSAria Fusion (Becton Dickinson) and FACSMelody (BD Biosciences).

Culture of PDX-derived AML cells

Cells were thawed in a 37°C water bath and washed once in Iscove's modified Dulbecco's medium (IMDM) supplemented with 10% FBS and 10 μ g/mL DNase I. Next, cells were placed in IMDM Glutamax supplemented with 20% of bovine serum albumin/insulin/transferrin (BIT) medium. BIT composition was: bovine serum albumin (BSA, Sigma-Aldrich, Cat# A9418) 4 g/L, Insulin 5 μ g/mL (Sigma-Aldrich, Cat# I2643) and Transferrin 60 μ g/mL (Sigma-Aldrich, Cat# T8158), 50 ng/mL FLT3 ligand (Cat# 300-19), 10 ng/mL IL-6 (Cat# 200-06), 50 ng/mL SCF (Cat# 300-07), 25 ng/mL TPO (Cat# 300-18), 10 ng/mL IL-3 (Cat# 200-03) and 10 ng/mL G-CSF (Cat# 300-23; all cytokines from Peprotech), 100 IU/mL penicillin, and 100 μ g/mL of streptomycin.

Gene expression profiling

Gene chip hybridization

RNA was extracted using a RNeasy Mini Kit (Qiagen, Redwood City, CA, USA) and quality was evaluated with a Bioanalyzer 2100 (using Agilent RNA6000 nano chip kit), and 100 ng of total RNA was reverse transcribed using the GeneChip® WT Plus Reagent Kit according to the manufacturer's instructions (Affymetrix, Thermo Fischer Scientific). Briefly, Double strand cDNA was used for in vitro transcription with T7 RNA polymerase and 5.5mg of Sens Target DNA was fragmented and labelled with biotin. cDNA were then hybridized to GeneChip® Clariom S Human (Affymetrix) at 45°C for 17 hours, then washed on the fluidic station FS450 (Affymetrix), and scanned using the GCS3000 7G (Thermo Fischer Scientific). Scanned

images were then analyzed with Expression Console software (Affymetrix, Thermo Fischer Scientific) to obtain raw data (.cel files) and metrics for quality controls.

Data processing and statistics

Raw fluorescence intensity values were normalized using Robust Multiarray Average (RMA) algorithm in R to generate the normalized data matrix by performing background correction, quantile normalization and log₂ transformation of raw fluorescence intensity values of each gene. All quality controls and statistics were performed using Partek® Genomics Suite software (Partek, St. Louis, MO, USA). Data were normalized using custom brainarray CDF files (v20 ENTREZG). To identify differentially expressed genes, we applied a classical analysis of variance (ANOVA) with a FDR permutation-base for each gene. We created a matrix with only the significant ANOVA site and performed Z-scoring of rows. Hierarchical clustering by Pearson's dissimilarity and average linkage and principal components analysis (PCA) were conducted in an unsupervised fashion to control for experimental bias or outlier samples. We set a filter for those genes that displayed at least a $\geq 1,5$ or $\leq -1,5$ fold difference in expression between groups and achieved an FDR of < 0.05 . Data were then interrogated for evidence of biologic pathway dysregulation using EnrichR userfriendly website (<https://maayanlab.cloud/Enrichr/>)(79–81) and Gene set enrichment analysis (GSEA, Broad Institute). Enrichment rates were considered as significant for p -value < 0.05

GSEA analysis

GSEA analysis was performed using GSEA version 4.1.0 (<https://www.gsea-msigdb.org/gsea/index.jsp>, BroadInstitute, RRID:SCR_003199)(82,83). Gene signatures used in this study were from Broad Institute database, literature, or in-house built. Following parameters were used: Number of permutations = 1000, permutation type = gene_set. Other parameters were left at default values.

RNA-sequencing

Library preparation

RNA sequencing library preparation was performed using Illumina TruSeq stranded mRNA protocol. The average number of reads per sample was 36 million. We mapped the reads to the human genome reference build hg38 using STAR aligner (STAR v2.6.1d, (84)). Detailed methods for RNA-seq quantification and differential gene expression analysis are provided in the Supplemental Material.

RNA-seq quantification

Transcript-level counts and transcripts per million (tpm) were estimated using Salmon 1.5.2, with default parameters. R (R version 4.1.2) package tximport (version 1.20.0, (85)) was used to summarize transcript-level estimates to the gene-level estimates.

Differential gene expression analysis

For plotting purpose, a variance stabilizing transformation (computed with the `vst()` function from DESeq2, version 1.34.0, (86)) was applied to the estimated counts from Salmon. As the samples were sequenced in different batches, the method `removeBatchEffect` (from the limma package, version 1.34.0, (87)) was further applied to remove the batch effect. For differential gene expression (DGE) analysis, raw counts were supplied to the R package DESeq2. As factors for the DGE analysis, we compared post-treatment versus pre-treatment samples grouped accordingly to the CEBPA signature expression level. Samples were labelled UP (or DOWN) if the CEBPA signature was up-regulated (or down-regulated) after treatment compared to the median of pre-treatment samples. The sequencing batch number was included as covariate to account for the batch effect. Hence, the resulting design formula supplied to DESeq2 was \sim treatment (post, pre) + CEBPA signature level (UP, DOWN) + batch. Post *versus* pre-treatment samples were compared for each CEBPA signature status (UP or DOWN). Differentially expressed genes were defined as genes with Benjamini-Hochberg-adjusted Wald test p-value < 0.1. Genes were ranked according to their log₂ fold-change in descending order and gene set enrichment analysis, GSEA (88) was performed with the GSEA function from the clusterProfiler R package (version 4.2.2, (89)).

Proteomics

Sample preparation

Cell pellets were resuspended in 100 μ l of 0.1 % RapiGest Surfactant (Waters) in 0.1M triethylammonium bicarbonate (TEAB). Samples were heated for 5 min at 95°C. Lysis was performed by sonication (6 x 30 sec.) at 70% amplitude and 0.5 pulse. Samples were kept 30 sec. on ice between each cycle of sonication. Samples were centrifuged for 5 min. at 17'000 x g. Remaining pellet was solubilized in 100 μ l of 0.1 % RapiGest, with 2 μ l of 0.1M MgCl₂ and 0.2 μ l of benzonase for DNA digestion. Protein lysates were pooled together and protein concentration was measured by Bradford assay and 25 μ g of each sample was subjected to protein digestion as follow: sample volume was adjusted to 100 μ l with 0.1M TEAB to obtain a final concentration of RapiGest 0.1%. 2 μ l of Dithioerythritol (DTE) 50 mM in distilled water were added and the reduction was carried out at 60°C for 1h. Alkylation was performed by adding 2 μ l of iodoacetamide (400 mM in distilled water) during 1 hour at room temperature in the dark. Overnight digestion was performed at 37 °C with 5 μ L of freshly prepared trypsin

(Promega; 0.1 µg/µl in TEAB 0.1M). To remove RapiGest, samples were acidified with TFA, heated at 37°C for 45 min. and centrifuged 10 min. at 17'000 x g. Supernatants were then desalted with a C18 microspin column (Harvard Apparatus) according to manufacturer's instructions, completely dried under speed-vacuum and stored at -20°C.

ESI-LC-MSMS

Samples were diluted in 25 µl of loading buffer (5% CH₃CN, 0.1% FA). Biognosys iRT peptides (1.5 µl) were added to each sample and 2 µl were injected on column. LC-ESI-MS/MS was performed on an Orbitrap Fusion Lumos Tribrid mass spectrometer (Thermo Fisher Scientific) equipped with an Easy nLC1200 liquid chromatography system (Thermo Fisher Scientific). Peptides were trapped on a Acclaim pepmap100, C18, 3µm, 75µm x 20mm nano trap-column (Thermo Fisher Scientific) and separated on a 75 µm x 500 mm, C18 ReproSil-Pur (Dr. Maisch GmbH), 1.9 µm, 100 Å, home-made column. The analytical separation was run for 135 min using a gradient of H₂O/FA 99.9%/0.1% (solvent A) and CH₃CN/H₂O/FA 80.0%/19.9%/0.1% (solvent B). Data-Independent Acquisition (DIA) was performed with MS1 full scan at a resolution of 60,000 (FWHM) followed by 30 DIA MS2 scan with variable windows. MS1 was performed in the Orbitrap with an AGC target of 1×10^6 , a maximum injection time of 50 ms and a scan range from 400 to 1240 m/z. DIA MS2 was performed in the Orbitrap using higher-energy collisional dissociation (HCD) at 30%. Isolation windows was set to 28 m/z with an AGC target of 1×10^6 and a maximum injection time of 54 ms.

Data analysis

DIA raw files were loaded into Spectronaut v.14 (Biognosys) and analysed by directDIA using default settings. Briefly, data were searched against Human reference proteome fasta database (Uniprot, release 2020_09, 55471 entries). Trypsin was selected as the enzyme, with one potential missed cleavage. Variable amino acid modifications were oxidized methionine and deaminated (NQ). Fixed amino acid modification was carbamidomethyl cysteine. Both peptide precursor and protein FDR were controlled at 1% (Q value < 0.01). Single Hit Proteins were excluded. For quantitation, Top 3 precursor area per peptides were used, "only protein group specific" was selected as proteotypicity filter and normalization was set to "global normalization". The quantitative analysis was performed with MapDIA tool, using the precursor quantities extracted from Spectronaut output. No further normalization was applied. The following parameters were used: min peptides = 2, max peptides = 10, min correl = -1, Min_DE = 0.01, max_DE = 0.99, and experimental_design = replicate design. Proteins were considered to have significantly changed in abundance with an FDR ≤ 0.05 and an absolute fold change $FC \geq |1.5|$ ($\log_2 FC \geq |0.58|$). FDR q-value was calculated using

the two-stage step-up method of Benjamini, Krieger and Yekutieli (Graphpad Prism, RRID:SCR_002798). Proteins were excluded when more than one replicate was impaired per condition. If only one replicate was impaired, it was excluded and the protein conserved.

Western blots

Cells were lysed in NuPAGE™ LDS Sample Buffer supplemented with NuPAGE™ Sample Reducing Agent (Life Technologies) and heated for 5 min at 90°C. Then proteins were separated using 4–12% gradient polyacrylamide SDS–PAGE gels (Life Technologies) and electrotransferred to 0.2 µm nitrocellulose membranes (GE Healthcare). After blocking in Tris-buffered saline with 0.2% Tween and 5% bovine serum albumin, membranes were blotted overnight at 4 °C with the appropriate primary antibodies. Primary antibodies were detected using the appropriate horseradish peroxidase-conjugated secondary antibodies. Immunoreactive bands were visualized by enhanced chemiluminescence (Thermo-Fisher Scientific, Cat# PI32209) with a Pxi camera (Syngene) using GeneSys software (Syngene, RRID:SCR_015770) or a fusion FX7 edge imaging System (Vilber) using Fusion FX software (Vilber). Protein levels were quantified using GeneTool software (Syngene) or Fusion FX software (Vilber, France) and normalized to nonvariable proteins such as Actin, GAPDH or HSP90. Primary antibodies used were: Actin (Cat# MAB1501, RRID:AB_2223041) was purchased from Millipore; AKT (Cat# 9272, RRID:AB_329827), Phospho-AKT (Ser493) (Cat# 9271, RRID:AB_329825), C/EBPα (Cat# 8178, RRID:AB_11178517), FASN (Cat# 3189, RRID:AB_2100798), FLT3 (Cat# 3462, RRID:AB_2107052), Phospho-FLT3 (Tyr591) (Cat# 3461, RRID:AB_331060), GAPDH (Cat# 5174, RRID:AB_10622025), HSP90 (Cat# 4874, RRID:AB_2121214), p44/p42 MAPK (ERK1/2) (Cat# 9102, RRID:AB_330744), Phospho-p44/42 MAPK (ERK1/2) (Thr202/Tyr204) (Cat# 9101, RRID:AB_331646), STAT5 (Cat# 94205, RRID:AB_2737403) and Phospho-STAT5 (Tyr694) (Cat# 9351, RRID:AB_2315225) were purchased from Cell Signaling Technology; FADS2 (Cat# ab72189, RRID:AB_2041175), GPX4 (Cat# ab41787, RRID:AB_941790), SREBP1 (Cat# ab28481, RRID:AB_778069), SREBP2 (Cat# ab30682, RRID:AB_779079) and SCD (Cat# ab19862, RRID:AB_445179) were purchased from Abcam.

Constructs

Expression vectors

We obtained human *CEBPA*, *SCD* and *FLT3*, as well as *CEBPA* S21A and S21D, and *FLT3*-ITD mutant open-reading frames (ORFs) through GeneArt gene synthesis technology (Thermo Fisher Scientific). *CEBPA* ORFs were cloned in pINDUCER21 (gift from Stephen Elledge & Thomas Westbrook (90); Addgene plasmid #46948; <http://n2t.net/addgene:46948>

; RRID:Addgene_46948). *SCD* ORF was cloned in pLenti PGK Puro DEST 5W(w529-2) (gift from Eric Campeau & Paul Kaufman (91); Addgene plasmid #19068; <http://n2t.net/addgene:19068> ; RRID:Addgene_19068). *FLT3* and *FLT3*-ITD ORFs were cloned in pLEX_307 (gift from David Root (Addgene plasmid #41392; <http://n2t.net/addgene:41392>; RRID: Addgene_41392))

RNA interference

We cloned shRNAs against *SCD* as well as control shRNA in the Tet-pLKO-puro vector (Gift from Dmitri Wiederschain, Addgene plasmid #21915; <http://n2t.net/addgene:21915>; RRID: Addgene_21915) allowing the conditional expression of hairpins by doxycycline. Sequences of shRNAs are (5'>3'): shCTL, CAACAAGATGAAGAGCACCAA; shSCD#1, CGTCCTTATGACAAGAACATT; shSCD#2, GCACATCAACTTCACCACATT.

For *FLT3* and *CEBPA* doxycycline-inducible invalidation, SMARTvector inducible human hEF1a-TurboGFP shRNA vectors purchased from Horizon Discovery. *FLT3*: shFLT3: Clone Id: V3IHSHEG_10441930, CTGGAGAATACCTACTTTT; Non-targeting Control hEF1a-TurboRFP, shCTL: Cat #VSC6573. *CEBPA*: pTRIPZ inducible vector (shCEBPA: RHS4696-200706732, clone ID: V2THS_14752, GGAAAGAATCAAGGAGG; shCTL: empty vector shRNA control, RHS4750).

For *CEBPA* constitutive invalidation, pLKO.1-puro constitutive vectors containing the following shRNA sequences were used (5' > 3'): shRNA control, purchased from Sigma-Aldrich (SHC002 MISSION pLKO.1-puro non-mammalian shRNA control; CCGGCAACAAGATGAAGAGCACCAACTC); shRNAs against *CEBPA*, purchased from Sigma-Aldrich (SHCLNG-NM_004364, TRCN0000007306 and TRCN0000356198).

Lentiviral production

Briefly, we transfected HEK 293T/17 cells with different plasmids together with the packaging plasmids pMD2.G (Gift from Didier Trono (Addgene plasmid #12259; <http://n2t.net/addgene:12259> ; RRID:Addgene_12259) and psPAX2 (Gift from Didier Trono (Addgene plasmid # 12260 ; <http://n2t.net/addgene:12260>; RRID:Addgene_12260) encoding lentiviral proteins using Lipofectamine 2000 Transfection Reagent (Thermo-Fischer Scientific). Twenty-four hours after cell transfection, medium was removed and Opti-MEM culture medium (Life Technology) was added. HEK 293T/17 culture supernatants containing lentiviral particles were harvested 72h after transduction, filtered, and used for lentiviral infection of AML cells or stored at -80 °C.

Lentiviral infection

On the day of transduction, 2×10^6 MOLM-14 or MV4-11 cells were seeded in a medium containing 8 $\mu\text{g}/\text{mL}$ polybrene (Sigma-Aldrich, Cat# 107689) and 2 mL of lentivirus-containing HEK 293T/17 supernatant. Three days after infection, transduced cells were selected using 1 $\mu\text{g}/\text{mL}$ puromycin (LabForce) or sorted on an Astrios cell sorter (Beckman Coulter) dependent on the vector.

Cell viability and synergy assays

AML cells were seeded at $2 \times 10^5/\text{ml}$ in 100 μl of 10% FBS-supplemented RPMI prior to the addition of compounds. Cells were cultured in the presence of the test compounds for 14h to 96 h at 37°C. Viability was quantified using the fluorescence based Alamar Blue assay (Invitrogen, Cat# DAL1025). Alamar blue was added to each well in 10 μl aliquots. Fluorescence was then measured with a spectramax paradigm microplate reader from Molecular Devices. Fluorescence values were normalized to DMSO-treated controls for each sample or cell line investigated.

To investigate potential synergy, dose-response matrices of QUIZ and MF-438 or RSL3 were done and cell viability was calculated for every dose combination using the Synergy Finder 2.0 (<https://synergyfinder.fimm.fi/>) (92) and compared to each agent alone. Calculations were based on the ZIP model. ZIP score interpretation: ZIP < -10, antagonist effect; -10 < ZIP < 10, additive effect; ZIP > 10, synergistic effect.

ATAC-seq sample preparation and analysis

Sample preparation and sequencing

shCTL and shC/EBP α MOLM14 cells (in biological duplicates) were FACS-sorted, and ATAC-seq was performed as previously described (93) with minor modifications. Briefly, 50 000 cells were lysed in ice-cold lysis buffer and the transposition reaction was performed using the Tn5 transposase at 37°C for 30 min. DNA was purified using the QIAGEN MinElute kit (QIAGEN). The libraries were prepared using Tagment DNA Enzyme and Buffer kits (Illumina), NEBNext High-Fidelity 2X PCR Master Mix (NEB, catalog # M0541S) with custom sequencing primers (94–97). The libraries were purified twice using AMPure XP beads (Beckman) following a double-sided protocol to remove primer dimers and large fragments. Libraries quality was assessed using the NGS High Sensitivity Kit on the Fragment Analyzer (Agilent Technologies, Santa Clara, USA). Only high-quality libraries were subsequently equimolarly pooled and sequencing was performed at the Pôle Technologique du CRCT – Plateau de Génomique et Transcriptomique (Inserm-UMR1037, Toulouse, France). The pool of libraries was quantified by qPCR using the KAPA Library Quantification Kit (Roche, Basel,

Switzerland) to obtain an accurate quantification. Sequencing was then performed on one flowcell of the Illumina NextSeq 550 instrument (Illumina, San Diego, USA), using the NextSeq 500/550 High Output Kit v2.5 (150 Cycles), and a paired-end 2 x 75 pb strategy. A minimum of 2x80 million raw reads were produced per sample.

Analysis

Adapter trimming and quality controls were performed using Trimgalore v0.6.5. and FastQC v0.11.7. Reads were aligned to the hg38 reference genome by using Bowtie2 v2.2.9. with the splicing alignment feature switched off. The chromatin-accessible peaks were called using Macs2 callpeaks v2.2.7.1 (q-value <0.01). The CHIPIN method and bedtools suite were used for normalisation and comparison.

Single cell RNA-sequencing

Purification of hCD45+CD33+ from PDX

After red blood cells lysis with EL buffer (Qiagen, 79217), 10×10^6 cells from mice bone marrow of PDXs treated with vehicle or GILT were stained with Fixable Viability Stain 510 (BD Biosciences Cat# 564406, RRID:AB_2869572) and the fluorescent conjugated antibodies hCD45-APC (BD Biosciences Cat# 555485, RRID:AB_398600) and hCD33-PE (BD Biosciences Cat# 555450, RRID:AB_395843) in cell staining buffer (Biolegend, BLE420201) following to the manufacturer's instructions. Viable hCD45+CD33+ were sorted using BD FACSAria Fusion flow cytometer (Becton Dickinson) and gently re-suspended at 1500cells/ μ L in PBS1X supplemented with 0.04% Ultrapure BSA (Invitrogen, Cat# AM2616).

Single cell library preparation and sequencing

Up to 10,000 cells per sample were encapsulated using the 10X Chromium controller (10X Genomics) following the Chromium Next GEM Single Cell 3' User Guide v3.1 (10X Genomics). Briefly, cells were encapsulated into oil droplets with barcoded Gel Beads and reagents to convert mRNA into complementary DNA (cDNA). cDNAs were then amplified, fragmented and Illumina adapters were added during ligation. After performing a last index PCR, libraries quality was assessed using TapeStation 2200 (Agilent) and frozen before quantitation and sequencing. Barcoding was done on three levels: cell barcodes allow attribution of each sequence read to its cell of origin; unique molecular identifiers (UMIs) upstream to poly(d)T primers allow tagging of each original molecule to avoid amplification bias; and index allows pooling of different samples. scRNA-seq libraries were quantified with HSD1000 reagents on TapeStation 2200 system (Agilent) and pooled at equimolar concentrations within 200 to 700bp. Pool libraries were sequenced at 1.8pM 1% phiX using a

NextSeq 500 sequencer (Illumina), at a sequencing depth of 40,000-50,000 reads per cell. Sequencing were configured Paired-End at 28 cycles for the first read, 91 cycles for the second one and 8 cycles for a single index.

Data analysis

Single cell RNA sequencing output bcl2 files were converted to FASTQ format by using Cell Ranger v.6.1.1.1(98). Count matrices from Cell Ranger were imported with the Seurat package v4.1.0(99) into the R programming environment v4.1.2. Cells that were deemed of lower quality were removed, based on their number of unique genes (<200 or >7500 unique genes) and the proportion of mitochondrial RNA (>20%). Gene counts were normalized with a regularized negative binomial regression, using the SCT normalization workflow from the Seurat package(100). In order to compare gene expression and signatures values after GILT treatment with those before treatment, the datasets from pre and post GILT treatment from each of the PDX sample were integrated following the Seurat dataset integration protocol(101). For dataset integration we used 30 principal components and 3000 genes. We then applied dimensional reduction where the 30 principal components were further summarized using UMAP dimensionality reduction. Cell clusters were identified using Louvain clustering within the Seurat workflow, the resolution parameter was set to 0.25. We identified clustering of co-expressing genes by hierarchical cluster with the package nclust (<https://gitlab.com/pwirapati/nclust>). We computed the values of the signatures on SCT transformed data with the AddModuleScore method from Seurat(102). The signature values were compared with UMAP and violin plots.

Lipidomic analysis of parental MOLM-14 and MV4-11

Sample preparation for untargeted lipidomics:

Cell lipid extracts were obtained from a frozen pellet of 4.10^{+6} harvested cells. Samples were resuspended in 70 μ L of ultrapure water, and then sonicated 5 times for 10 s using a sonication probe (vibra cell). At this step, 20 μ L of each sample were withdrawn for further determining the total protein concentration (colorimetric quantification / Pierce BCA Protein Assay Kit, Thermo Fisher Scientific). Samples were extracted using an adapted method previously described(103). Briefly, volumes of CHCL₃/MeOH 2:1 (v/v) were adjusted depending total protein concentration at 3.5 μ g/ μ l in addition to internal standards. Samples were vortexed for 60 s, sonicated for 30 s using an ultrasonic probe (Bioblock Scientific Vibra Cell VC 75,185, Thermo Fisher Scientific) and incubated for 2 h at 4 °C with mixing. According to volumes of CHCL₃/MeOH 2:1 (v/v), H₂O was then added and samples were vortexed for 60 s before centrifugation at 15,000 g for 15 min at 4 °C. The upper phase

(aqueous phase), containing gangliosides, lysoglycerophospholipids, and short chain glycerophospholipids, was transferred into a glass tube and dried under a stream of nitrogen. The protein disk interphase was discarded and the lower lipid-rich phase (organic phase) was pooled with the dried upper phase and the mixture dried under nitrogen. All samples were resuspended in the same initial volume of CHCL₃/MeOH 2:1 (v/v) and 40 µl of each extract was 5-fold diluted in a solution of MeOH/isopropanol/H₂O 65:35:5 (v/v/v) before injection. A quality control (QC) sample was obtained by pooling 20 µL of each sample preparation. QC samples was injected every 10 samples in order to evaluate the signal variations of lipid species.

Untargeted lipidomics and data processing

Lipidomic profiles were determined using an Ultimate 3000 liquid chromatography system (Thermo Fisher Scientific) coupled to a high resolution Thermo Orbitrap Fusion (Thermo Fisher Scientific) equipped with an electrospray source (ESI). Chromatographic separation was performed on a Phenomenex Kinetex C8 column (150 x 2.1 mm, 2.6 µm) at 0.4 mL/min, 60 °C and using an injection volume of 10 µL. Mobile phases A and B were H₂O/ MeOH 60:40 (v/v), 0.1% formic acid and isopropanol/MeOH 90:10 (v/ v), 0.1% formic acid in negative ionization mode, respectively. Ammonium formate (10 mM) was added to both mobile phases in the positive ionization mode in order to detect glycerolipids and cholesteryl-esters under [M+NH₄]⁺ form. The gradient elution was solvent B was maintained for 2.5 min at 32%, from 2.5 to 3.5 min it was increased to 45% B, from 3.5 to 5 min to 52% B, from 5 to 7 min to 58% B, from 7 to 10 min to 66% B, from 10 to 12 min to 70% B, from 12 to 15 min to 75% B, from 15 to 19 min to 80% B, from 19 to 22 min to 85% B, and from 22 to 23 min to 95% B; from 23 to 25 min, 95% B was maintained; from 25 to 26 min solvent B was decreased to 32% and then maintained for 4 min for column re-equilibration. The mass resolving power of the mass spectrometer was 240,000 (FWHM) for MS experiments. Samples were analyzed in both positive and negative ionization modes. The ESI source parameters were as follows: the spray voltage was set to 3.7 kV and -3.2 kV in positive and negative ionization mode, respectively. The heated capillary was kept at 360 °C and the sheath and auxiliary gas flow were set to 50 and 15 (arbitrary units), respectively. Mass spectra were recorded in full-scan MS mode from m/z 50 to m/z 2000. After LC-HRMS analysis of samples and annotation of features, QC samples were re-injected for higher energy collisional dissociation (HCD) MS/MS experiments in positive and negative ion modes on the same instrument set in targeted mode using inclusion lists. The isolation width was set at m/z 0.8, the stepped normalized collision energy was set at 20 % ± 10 % and the mass resolution was set at 17 500 FWHM at m/z 200. HCD mass spectra were inspected manually in order to confirm annotations.

Obtained Raw files were converted to the mzML or mzXML format with the ProteoWizard software(104). Mass spectra were processed using the xcms R package deployed in the Workflow4Metabolomics Galaxy platform(105) (<https://workflow4metabolomics.org>). Features were annotated by using an in-house database based on accurate measured masses and several filtration steps such as retention time windows depending lipid classes and relative isotopic abundance (RIA) of lipid species in order to limit false annotations for lipidomics.

Lipidomic analysis of MOLM-14 cells depleted from or overexpressing CEBPA

Lipid extraction

An amount of cells containing 10 µg of DNA was homogenized in 700 µL of water with a handheld sonicator and was mixed with 800 µl HCl(1M):CH₃OH 1:8 (v/v), 900 µl CHCl₃, 200 µg/ml of the antioxidant 2,6-di-tert-butyl-4-methylphenol (BHT, Sigma-Aldrich, Cat# B1378) and 3 µl of SPLASH® LIPIDOMIX® Mass Spec Standard (Avanti Polar Lipids, Cat# 330707). After vortexing and centrifugation, the lower organic fraction was collected and evaporated using a Savant Speedvac spd111v (Thermo Fisher Scientific) at room temperature and the remaining lipid pellet was stored at -20°C under argon.

Mass spectrometry

Just before mass spectrometry analysis, lipid pellets were reconstituted in 100% ethanol. Lipid species were analyzed by liquid chromatography electrospray ionization tandem mass spectrometry (LC-ESI/MS/MS) on a Nexera X2 UHPLC system (Shimadzu) coupled with hybrid triple quadrupole/linear ion trap mass spectrometer (6500+ QTRAP system; AB SCIEX). Chromatographic separation was performed on a XBridge amide column (150 mm × 4.6 mm, 3.5 µm; Waters) maintained at 35°C using mobile phase A [1 mM ammonium acetate in water-acetonitrile 5:95 (v/v)] and mobile phase B [1 mM ammonium acetate in water-acetonitrile 50:50 (v/v)] in the following gradient: (0-6 min: 0% B → 6% B; 6-10 min: 6% B → 25% B; 10-11 min: 25% B → 98% B; 11-13 min: 98% B → 100% B; 13-19 min: 100% B; 19-24 min: 0% B) at a flow rate of 0.7 mL/min which was increased to 1.5 mL/min from 13 minutes onwards. SM, CE, CER, DCER, HCER, LCER were measured in positive ion mode with a precursor scan of 184.1, 369.4, 264.4, 266.4, 264.4 and 264.4 respectively. TAG, DAG and MAG were measured in positive ion mode with a neutral loss scan for one of the fatty acyl moieties. PC, LPC, PE, LPE, PG, PI and PS were measured in negative ion mode by fatty acyl fragment ions. Lipid quantification was performed by scheduled multiple reactions monitoring (MRM), the transitions being based on the neutral losses or the typical product ions as described above. The instrument parameters were as follows: Curtain Gas =

35 psi; Collision Gas = 8 a.u. (medium); IonSpray Voltage = 5500 V and -4,500 V; Temperature = 550°C; Ion Source Gas 1 = 50 psi; Ion Source Gas 2 = 60 psi; Declustering Potential = 60 V and -80 V; Entrance Potential = 10 V and -10 V; Collision Cell Exit Potential = 15 V and -15 V.

The following fatty acyl moieties were taken into account for the lipidomic analysis: 14:0, 14:1, 16:0, 16:1, 16:2, 18:0, 18:1, 18:2, 18:3, 20:0, 20:1, 20:2, 20:3, 20:4, 20:5, 22:0, 22:1, 22:2, 22:4, 22:5 and 22:6 except for TGs which considered: 16:0, 16:1, 18:0, 18:1, 18:2, 18:3, 20:3, 20:4, 20:5, 22:2, 22:3, 22:4, 22:5, 22:6.

Data Analysis

Peak integration was performed with the MultiQuant™ software version 3.0.3. Lipid species signals were corrected for isotopic contributions (calculated with Python Molmass 2019.1.1) and were quantified based on internal standard signals and adheres to the guidelines of the Lipidomics Standards Initiative (LSI) (level 2 type quantification as defined by the LSI). Unpaired t-test p-values was calculated in Python StatsModels version 0.10.1. Lipid species were considered to have significantly changed in abundance with an FDR ≤ 0.05 and an absolute fold change $FC \geq |1.5|$ ($\log_2 FC \geq |0.58|$). Lipid species were excluded when more than one replicate was impaired per condition. If only one replicate was impaired, it was excluded and the lipid species conserved. PUFA:MUFA ratios for each phospholipid subclasses were calculated using this formula:

$$\frac{PUFA}{MUFA} = \frac{\Sigma (\text{relative quantity of PUFA from 2 to 6 saturations})}{\text{relative quantity of MUFA}}$$

Fatty acids isotopic labeling profiling

Sample preparation

MV4-11 and MOLM-14 cells were plated at 0.4×10^6 cells per mL and treated with QUIZ in media supplemented with U-¹³C₆-glucose (5.6 mM) or U-¹³C₅-glutamine (2 mM) for 24 h before sampling. Lipids corresponding total FA from cell pellets of three million cells of three independent experiments were extracted according to Bligh and Dyer(106) in dichloromethane/water/methanol 2% acetic acid (2.5:2.5:2, v/v/v), in the presence of the internal standards glyceryl trinonadecanoate (4µg). After centrifugation during 6min at 2500 rpm, the lipid extract was hydrolysed in KOH (0.5 M in methanol, 1mL) at 55°C for 30 min. A second extraction was performed with dichloromethane/water/methanol (2.5/2/1.5, v/v/v). The lipid extract was evaporated to dryness and dissolved in ethyl acetate (10 µL).

Derivatization was performed with PentafluoroBenzylBromide in ACN (1%) and Diisopropylethylamine in ACN (1%) (1/1, v/v).

GC-MS Analysis

Fatty acid methyl ester (1 μ L) were analyzed on a gas chromatography Thermo Trace 1310 (Thermo Fisher Scientific) with mass spectrometer Thermo TSQ 8000 EVO (Thermo Fisher Scientific). Chemical ionization is used as ionization, helium as carrier gas, and a HP-5MS column (30 m x 0.25 mm, 0.25 μ m) is used to separation. Oven temperature was programmed from 130°C to 232°C at a rate of 4°C/min (8 min), from 232°C to 230°C at a rate of 10°C/min (2 min). A full scan method was used to detected compounds.

Data Processing

GC-MS analysis produced a mass spectrum for each FA, which contains the abundance of each isotopologue. For each FA, the lightest (unlabeled) isotopologue is denoted M + 0 whereas the isotopologue with 1 atom [^{13}C] PFB-palmitate (M+1) has a mass of 256.3, etc. Isotopic clusters were obtained by integrating gas chromatographic signals for each isotopologue. Isotopologue distributions were obtained from the corresponding isotopic clusters after correction for natural abundance of carbon and non-tracer elements (oxygen and hydrogen) using IsoCor software(107) (<https://isocor.readthedocs.io/en/latest/index.html>), and purity of the tracer was corrected assuming 99% ^{13}C -purity. Finally, the ^{13}C -enrichment, which represents the mean content in tracer atoms (^{13}C) within the molecule, was calculated from the corresponding IDs.

Flow cytometry

We measured lipid peroxide production using 2 μ M C11-BODIPY (581/591) (Invitrogen, Cat# D3861) according to manufacturer's instructions. We used either Annexin-V APC (Cat# 550474), FITC (Cat# 556420), BV421 (Cat# 563973) or V500 (Cat# 561501), all from BD Biosciences), or Propidium iodide (Invitrogen, Cat# P1304MP), or DRAQ7 (Thermo-Fischer Scientific, Cat# D15106) to measure cell viability, according to the manufacturer's instructions. Data were collected using a C6 Accuri flow cytometer (Becton Dickinson) with CFlow Plus software or using CytoFLEX flow cytometer (Beckman Coulter). We used CFlow Plus (Becton Dickinson) or FlowJo software (Becton Dickinson, RRID:SCR_008520) for analysis of at least 10⁴ cells per condition.

4-hydroxynonenal (4-HNE) measurement

Femurs, tibias and spleens of mice were fixed for 24h in 4% paraformaldehyde. Decalcification was carried out using 15% formic acid at 4°C for 4h, followed by a second fixation in 4% paraformaldehyde during 24h. Samples were paraffin embedded and then sliced using a microtome. Serial sections (4 µm) were analyzed by immunohistochemistry using a polyclonal anti-4-HNE antibody (Thermo-Fisher Scientific, Cat# BS-6313R) according to manufacturer's instructions. Briefly, slides have been heated in a microwave submersed in 1X citrate unmasking solution until boiling, follow with 10 min at sub-boiling temperature (95°-98°). After Cooling and washing, sections were blocked for 1 hr at room temperature, and incubated with anti-4-HNE antibody (1/100 dilution) overnight at 4°C. After removing antibody solution, sections were covered with the SignalStain® Boost IHC Detection Reagent (HRP, Rabbit, Cell Signaling Technologies, Cat #8114) for 30 min. Next, stained slides were imaged using the Widefield scanner Axioscan.Z1 slide scanner (Zeiss) and quantification of 4-HNE signal was done using the QuPath software (108).

Statistics

Statistical analyses were conducted using GraphPad Prism software v9.2.0 (RRID:SCR_002798). For *in vitro* studies, statistical significance was determined by the two-tailed unpaired Student's t test with Welch's correction, or paired t-test or ratio paired t-test when appropriate. For *in vivo* studies, statistical significance was determined by the non-parametric Mann-Whitney test. Unless otherwise indicated, all data represent the mean ± SD from at least three independent experiments. *p<0.05, **p<0.01, ***p<0.001.

DATA AVAILABILITY STATEMENT

Further information, resources and reagents are available upon request. Inquiries should be directed to and will be fulfilled by Jean-Emmanuel Sarry (jean-emmanuel.sarry@inserm.fr) and Jerome Tamburini (jerome.tamburinibonnefoy@unige.ch).

Microarray, bulk RNA-seq, single cell RNA-seq and ATAC-seq data are publicly available in Gene Expression Omnibus (GEO) at GSE226461, GSE227839, GSE227874, and GSE227400, respectively. All additional data reported in this paper will be shared by the lead contacts upon request. Any additional information required to reanalyze the data reported in this paper is available from the lead contacts upon request.

ACKNOWLEDGMENTS

We thank all members of mice core facilities (UMS006, ANEXPLO, Inserm, Toulouse) in particular Marie Lulka, Christine Campi and Cédric Baudelin for their support and technical assistance. We thank Anne-Marie Benot, Muriel Serthelon and Stéphanie Nevouet for their daily help about the administrative and financial management of our Team. We thank the Geneva University Medical School electron microscopy (PFMU), flow cytometry, bioimaging, genomics (iGE3), proteomics, Reader Assay Development and Screening (READS) and zootechnie core facilities for technical support. The authors also wish to thank the Barts Cancer Institute tissue bank for sample collection and processing. This research was supported Cancer Research UK (PG, Advanced Clinician Scientist fellowship, C57799/A27964).

This work was supported by grants from the Laboratoire d'Excellence Toulouse Cancer (TOUCAN and TOUCAN2.0; contract ANR11-LABEX), INCA (PLBIO 2020-010, DIALAML), the Fondation Toulouse Cancer Santé, the Ligue National de Lutte Contre le Cancer, the European Regional Development Fund (ERDF; the Interreg V-A Spain-France-Andorra (POCTEFA) program, EFA360/19), the Fondation ARC, and the association GAEL. M.S. and R.B. were fellows from the Fondation ARC contre le Cancer. L.L is supported by a PhD fellowship from the Ligue National de Lutte Contre le Cancer. A.S. is a fellow from the European Regional Development Fund (ERDF) through the Interreg V-A Spain-France-Andorra (POCTEFA) program, project PROTEOblood (EFA360/19). This work was also supported by grants from the Dr. Henri Dubois-Ferrière, Dinu Lipatti Fondation and Geneva university hospital private Foundation. This work was also supported by funding from Ligue Genevoise contre le Cancer, Fondation Copley May, Fondation Medic and Fondation Pastré through the Translational Research Center for Hemato-Oncology (University of Geneva, Faculty of Medicine, Geneva, Switzerland). METATOUL-lipidomics core facility is a member of the MetaboHUB French infrastructure (ANR-INBS-0010). Team JE Sarry and Team D Bouscary are members of OPALE Carnot Institute, The Organization for Partnerships in Leukemia.

REFERENCES

1. Papaemmanuil E, Gerstung M, Bullinger L, Gaidzik VI, Paschka P, Roberts ND, et al. Genomic Classification and Prognosis in Acute Myeloid Leukemia. *New England Journal of Medicine*. N Engl J Med; 2016;374:2209–21.
2. Thiede C, Steudel C, Mohr B, Schaich M, Schäkel U, Platzbecker U, et al. Analysis of FLT3-activating mutations in 979 patients with acute myelogenous leukemia: Association with FAB subtypes and identification of subgroups with poor prognosis. *Blood*. Blood; 2002;99:4326–35.
3. Kottaridis PD, Gale RE, Frew ME, Harrison G, Langabeer SE, Belton AA, et al. The presence of a FLT3 internal tandem duplication in patients with acute myeloid leukemia (AML) adds important prognostic information to cytogenetic risk group and response to the first cycle of chemotherapy: Analysis of 854 patients from the United King. *Blood*. 2001;98:1752–9.
4. Tiesmeier J, Müller-Tidow C, Westermann A, Czwalinna A, Hoffmann M, Krauter J, et al. Evolution of FLT3-ITD and D835 activating point mutations in relapsing acute myeloid leukemia and response to salvage therapy. *Leukemia Research*. Pergamon; 2004;28:1069–74.
5. Bjelosevic S, Gruber E, Newbold A, Shembrey C, Devlin JR, Hogg SJ, et al. Serine biosynthesis is a metabolic vulnerability in flt3-itd-driven acute myeloid leukemia. *Cancer Discovery*. American Association for Cancer Research; 2021;11:1582–99.
6. Gregory MA, D'Alessandro A, Alvarez-Calderon F, Kim J, Nemkov T, Adane B, et al. ATM/G6PD-driven redox metabolism promotes FLT3 inhibitor resistance in acute myeloid leukemia. *Proceedings of the National Academy of Sciences of the United States of America*. 2016;113:E6669–78.
7. Ju HQ, Zhan G, Huang A, Sun Y, Wen S, Yang J, et al. ITD mutation in FLT3 tyrosine kinase promotes Warburg effect and renders therapeutic sensitivity to glycolytic inhibition. *Leukemia*. 2017;31:2143–50.
8. Gallipoli P, Giotopoulos G, Tzelepis K, Costa ASH, Vohra S, Medina-Perez P, et al. Glutaminolysis is a metabolic dependency in FLT3 ITD acute myeloid leukemia unmasked by FLT3 tyrosine kinase inhibition. *Blood*. 2018;131:1639–53.
9. Zavorka Thomas ME, Lu X, Talebi Z, Jeon JY, Buelow DR, Gibson AA, et al. Gilteritinib Inhibits Glutamine Uptake and Utilization in FLT3-ITD-Positive AML. *Mol Cancer Ther*. 2021;20:2207–17.
10. Stone RM, Mandrekar SJ, Sanford BL, Laumann K, Geyer S, Bloomfield CD, et al. Midostaurin plus Chemotherapy for Acute Myeloid Leukemia with a FLT3 Mutation. *New England Journal of Medicine*. Massachusetts Medical Society; 2017;377:454–64.
11. Perl AE, Martinelli G, Cortes JE, Neubauer A, Berman E, Paolini S, et al. Gilteritinib or Chemotherapy for Relapsed or Refractory FLT3 -Mutated AML. *New England Journal of Medicine*. 2019;381:1728–40.
12. Sato T, Yang X, Knapper S, White P, Smith BD, Galkin S, et al. FLT3 ligand impedes the efficacy of FLT3 inhibitors in vitro and in vivo. *Blood*. Blood; 2011;117:3286–93.
13. Kojima K, McQueen T, Chen Y, Jacamo R, Konopleva M, Shinojima N, et al. p53 activation of mesenchymal stromal cells partially abrogates microenvironment-mediated resistance to FLT3 inhibition in AML through HIF-1 α -mediated down-regulation of CXCL12. *Blood*. Blood; 2011;118:4431–9.
14. Traer E, Martinez J, Javidi-Sharifi N, Agarwal A, Dunlap J, English I, et al. FGF2 from marrow microenvironment promotes resistance to FLT3 inhibitors in acute myeloid leukemia. *Cancer Research*. Cancer Res; 2016;76:6471–82.
15. Dumas PY, Naudin C, Martin-Lannerée S, Izac B, Casetti L, Mansier O, et al. Hematopoietic niche drives FLT3-ITD acute myeloid leukemia resistance to quizartinib via STAT5- And hypoxia-dependent upregulation of AXL. *Haematologica*. Ferrata Storti

Foundation; 2019;104:2017–27.

16. Javidi-Sharifi N, Martinez J, English I, Joshi SK, Scopim-Ribiero R, Edwards V DK, et al. Fgf2-fgfr1 signaling regulates release of leukemia-protective exosomes from bone marrow stromal cells. *eLife*. eLife Sciences Publications Ltd; 2019;8.
17. Joshi SK, Nechiporuk T, Bottomly D, Pichowski PD, Reisz JA, Pittsenbarger J, et al. The AML microenvironment catalyzes a stepwise evolution to gilteritinib resistance. *Cancer Cell*. 2021;39:999-1014.e8.
18. Smith CC, Levis MJ, Perl AE, Martinelli G, Neubauer A, Berman E, et al. Emerging Mutations at Relapse in Patients with FLT3-Mutated Relapsed/Refractory Acute Myeloid Leukemia Who Received Gilteritinib Therapy in the Phase 3 Admiral Trial. *Blood*. American Society of Hematology; 2019;134:14–14.
19. McMahon CM, Ferng T, Canaani J, Wang ES, Morrissette JJD, Eastburn DJ, et al. Clonal selection with RAS pathway activation mediates secondary clinical resistance to selective FLT3 inhibition in acute myeloid leukemia. *Cancer Discovery*. *Cancer Discov*; 2019;9:1050–63.
20. Alotaibi AS, Yilmaz M, Kanagal-Shamanna R, Loghavi S, Kadia TM, DiNardo CD, et al. Patterns of Resistance Differ in Patients with Acute Myeloid Leukemia Treated with Type I versus Type II FLT3 Inhibitors. *Blood Cancer Discovery*. *American Association for Cancer Research Journals*; 2021;2:125–34.
21. Avellino R, Delwel R. Expression and regulation of C/EBP α in normal myelopoiesis and in malignant transformation. *Blood*. 2017;129:2083–91.
22. Taube F, Georgi JA, Kramer M, Stasik S, Middeke JM, Röllig C, et al. CEBPA mutations in 4708 patients with acute myeloid leukemia: differential impact of bZIP and TAD mutations on outcome. *Blood*. *Blood*; 2022;139:87–103.
23. Pabst T, Mueller BU, Harakawa N, Schoch C, Haferlach T, Behre G, et al. AML1-ETO downregulates the granulocytic differentiation factor C/EBP α in t(8;21) myeloid leukemia. *Nature Medicine*. *Nature Publishing Group*; 2001;7:444–51.
24. Christy RJ, Yang VW, Ntambi JM, Geiman DE, Landschulz WH, Friedman AD, et al. Differentiation-induced gene expression in 3T3-L1 preadipocytes: CCAAT/enhancer binding protein interacts with and activates the promoters of two adipocyte-specific genes. *Genes & development*. *Genes Dev*; 1989;3:1323–35.
25. Tae HJ, Luo X, Kim KH. Roles of CCAAT/enhancer-binding protein and its binding site on repression and derepression of acetyl-CoA carboxylase gene. *Journal of Biological Chemistry*. 1994;269:10475–84.
26. Pedersen TÅ, Bereshchenko O, Garcia-Silva S, Ermakova O, Kurz E, Mandrup S, et al. Distinct C/EBP α motifs regulate lipogenic and gluconeogenic gene expression in vivo. *EMBO Journal*. 2007;26:1081–93.
27. Spiekermann K, Bagrintseva K, Schwab R, Schmieja K, Hiddemann W. Overexpression and constitutive activation of FLT3 induces STAT5 activation in primary acute myeloid leukemia blast cells. *Clinical Cancer Research*. 2003;9:2140–50.
28. Brandts CH, Sargin B, Rode M, Biermann C, Lindtner B, Schwäble J, et al. Constitutive activation of Akt by Flt3 internal tandem duplications is necessary for increased survival, proliferation, and myeloid transformation. *Cancer Research*. 2005;65:9643–50.
29. Chen W, Drakos E, Grammatikakis I, Schlette EJ, Li J, Leventaki V, et al. MTOR signaling is activated by FLT3 kinase and promotes survival of FLT3-mutated acute myeloid leukemia cells. *Molecular Cancer*. *BioMed Central*; 2010;9:1–7.
30. Gregory MA, Nemkov T, Park HJ, Zaberezhnyy V, Gehrke S, Adane B, et al. Targeting glutamine metabolism and redox state for leukemia therapy. *Clinical Cancer Research*. *Clin Cancer Res*; 2019;25:4079–90.
31. Guillou H, Zadravec D, Martin PGP, Jacobsson A. The key roles of elongases and desaturases in mammalian fatty acid metabolism: Insights from transgenic mice. *Progress in*

- Lipid Research. *Prog Lipid Res*; 2010. page 186–99.
32. Tyner JW, Tognon CE, Bottomly D, Wilmot B, Kurtz SE, Savage SL, et al. Functional genomic landscape of acute myeloid leukaemia. *Nature*. 2018;562:526–31.
 33. Cancer Genome Atlas Research Network, Ley TJ, Miller C, Ding L, Raphael BJ, Mungall AJ, et al. Genomic and epigenomic landscapes of adult de novo acute myeloid leukemia. *N Engl J Med*. 2013;368:2059–74.
 34. Verhaak RGW, Wouters BJ, Erpelinck CAJ, Abbas S, Beverloo HB, Lugthart S, et al. Prediction of molecular subtypes in acute myeloid leukemia based on gene expression profiling. *Haematologica*. 2009;94:131–4.
 35. Decroocq J, Birsén R, Montersino C, Chaskar P, Mano J, Poulain L, et al. RAS activation induces synthetic lethality of MEK inhibition with mitochondrial oxidative metabolism in acute myeloid leukemia. *Leukemia*. 2022;36:1237–52.
 36. Cambridge SB, Gnad F, Nguyen C, Bermejo JL, Krüger M, Mann M. Systems-wide proteomic analysis in mammalian cells reveals conserved, functional protein turnover. *J Proteome Res*. 2011;10:5275–84.
 37. Radomska HS, Bassères DS, Zheng R, Zhang P, Dayaram T, Yamamoto Y, et al. Block of C/EBP α function by phosphorylation in acute myeloid leukemia with FLT3 activating mutations. *Journal of Experimental Medicine*. Rockefeller University Press; 2006;203:371–81.
 38. Radomska HS, Alberich-Jordà M, Will B, Gonzalez D, Delwel R, Tenen DG. Targeting CDK1 promotes FLT3-activated acute myeloid leukemia differentiation through C/EBP α . *Journal of Clinical Investigation*. 2012;122:2955–66.
 39. Shimano H, Sato R. SREBP-regulated lipid metabolism: Convergent physiology-divergent pathophysiology. *Nature Reviews Endocrinology*. *Nat Rev Endocrinol*; 2017. page 710–30.
 40. Bjelosevic S, Gruber E, Newbold A, Shembrey C, Devlin JR, Hogg SJ, et al. Serine Biosynthesis Is a Metabolic Vulnerability in FLT3-ITD-Driven Acute Myeloid Leukemia. *Cancer Discov*. 2021;11:1582–99.
 41. Butler LM, Perone Y, Dehairs J, Lupien LE, de Laat V, Talebi A, et al. Lipids and cancer: Emerging roles in pathogenesis, diagnosis and therapeutic intervention. *Advanced Drug Delivery Reviews*. 2020. page 245–93.
 42. Jiang X, Stockwell BR, Conrad M. Ferroptosis: mechanisms, biology and role in disease. *Nature Reviews Molecular Cell Biology*. 2021. page 266–82.
 43. Magtanong L, Ko P-J, To M, Cao JY, Forcina GC, Tarangelo A, et al. Exogenous Monounsaturated Fatty Acids Promote a Ferroptosis-Resistant Cell State. *Cell Chem Biol*. 2019;26:420-432.e9.
 44. Yang WS, Sriramaratnam R, Welsch ME, Shimada K, Skouta R, Viswanathan VS, et al. Regulation of ferroptotic cancer cell death by GPX4. *Cell*. 2014;156:317–31.
 45. Hayakawa F, Towatari M, Kiyoi H, Tanimoto M, Kitamura T, Saito H, et al. Tandem-duplicated Flt3 constitutively activates STAT5 and MAP kinase and introduces autonomous cell growth in IL-3-dependent cell lines. *Oncogene*. 2000;19:624–31.
 46. Tse KF, Novelli E, Civin CI, Bohmer FD, Small D. Inhibition of FLT3-mediated transformation by use of a tyrosine kinase inhibitor. *Leukemia*. 2001;15:1001–10.
 47. Léger S, Black WC, Deschenes D, Dolman S, Falguyret JP, Gagnon M, et al. Synthesis and biological activity of a potent and orally bioavailable SCD inhibitor (MF-438). *Bioorganic and Medicinal Chemistry Letters*. *Bioorg Med Chem Lett*; 2010;20:499–502.
 48. Gaschler MM, Andia AA, Liu H, Csuka JM, Hurlocker B, Vaiana CA, et al. FINO2 initiates ferroptosis through GPX4 inactivation and iron oxidation. *Nat Chem Biol*. 2018;14:507–15.
 49. Sallman DA, DeZern AE, Garcia-Manero G, Steensma DP, Roboz GJ, Sekeres MA, et al. Eprentapopt (APR-246) and azacitidine in TP53-mutant myelodysplastic syndromes.

- Journal of Clinical Oncology. *J Clin Oncol*; 2021. page 1584–94.
50. Tessoulin B, Descamps G, Moreau P, Maïga S, Lodé L, Godon C, et al. PRIMA-1Met induces myeloma cell death independent of p53 by impairing the GSH/ROS balance. *Blood*. 2014;124:1626–36.
 51. Bykov VJN, Zhang Q, Zhang M, Ceder S, Abrahmsen L, Wiman KG. Targeting of mutant P53 and the cellular redox balance by APR-246 as a strategy for efficient cancer therapy. *Frontiers in Oncology*. *Frontiers*; 2016. page 21.
 52. Liu DS, Duong CP, Haupt S, Montgomery KG, House CM, Azar WJ, et al. Inhibiting the system xC⁻/glutathione axis selectively targets cancers with mutant-p53 accumulation. *Nature Communications*. *Nat Commun*; 2017;8.
 53. Birsén R, Larrue C, Decroocq J, Johnson N, Guiraud N, Gotanegre M, et al. APR-246 induces early cell death by ferroptosis in acute myeloid leukemia. *Haematologica*. *Haematologica*; 2022;107:403–16.
 54. Fujihara KM, Benitez MC, Cabalag CS, Zhang BZ, Ko HS, Liu DS, et al. SLC7A11 Is a Superior Determinant of APR-246 (Eprexapopt) Response than TP53 Mutation Status. *Molecular Cancer Therapeutics*. American Association for Cancer Research Inc.; 2021;20:1858–67.
 55. Burchert A, Bug G, Fritz L V., Finke J, Stelljes M, Röllig C, et al. Sorafenib maintenance after allogeneic hematopoietic stem cell transplantation for acute myeloid leukemia with FLT3-internal tandem duplication mutation (SORMAIN). *Journal of Clinical Oncology*. American Society of Clinical Oncology; 2020;38:2993–3002.
 56. Smith CC, Wang Q, Chin C-S, Salerno S, Damon LE, Levis MJ, et al. Validation of ITD mutations in FLT3 as a therapeutic target in human acute myeloid leukaemia. *Nature* 2012 485:7397. *Nature Publishing Group*; 2012;485:260–3.
 57. Green AS, Maciel TT, Hospital MA, Yin C, Mazed F, Townsend EC, et al. Pim kinases modulate resistance to FLT3 tyrosine kinase inhibitors in FLT3-ITD acute myeloid leukemia. *Science Advances*. *Sci Adv*; 2015;1.
 58. Stockard B, Garrett T, Guingab-Cagmat J, Meshinchi S, Lamba J. Distinct Metabolic features differentiating FLT3-ITD AML from FLT3-WT childhood acute myeloid leukemia. *Scientific Reports*. 2018;8.
 59. Ogretmen B. Sphingolipid metabolism in cancer signalling and therapy. *Nature Reviews Cancer*. 2017. page 33–50.
 60. Dany M, Gencer S, Nganga R, Thomas RJ, Oleinik N, Baron KD, et al. Targeting FLT3-ITD signaling mediates ceramide-dependent mitophagy and attenuates drug resistance in AML. *Blood*. 2016;128:1944–58.
 61. Gouazé V, Mirault ME, Carpentier S, Salvayre R, Levade T, Andrieu-Abadie N. Glutathione peroxidase-1 overexpression prevents ceramide production and partially inhibits apoptosis in doxorubicin-treated human breast carcinoma cells. *Molecular Pharmacology*. *Mol Pharmacol*; 2001;60:488–96.
 62. Hermetet F, Mshaik R, Simonet J, Callier P, Delva L, Quéré R. High-fat diet intensifies MLL-AF9-induced acute myeloid leukemia through activation of the FLT3 signaling in mouse primitive hematopoietic cells. *Scientific Reports*. *Sci Rep*; 2020;10.
 63. Stuani L, Sabatier M, Saland E, Cognet G, Poupin N, Bosc C, et al. Mitochondrial metabolism supports resistance to IDH mutant inhibitors in acute myeloid leukemia. *Journal of Experimental Medicine*. The Rockefeller University Press; 2021;218.
 64. Flowers MT, Ntambi JM. Role of stearoyl-coenzyme A desaturase in regulating lipid metabolism. *Current Opinion in Lipidology*. 2008. page 248–56.
 65. Puca F, Yu F, Bartolacci C, Pettazzoni P, Carugo A, Huang-Hobbs E, et al. Medium-chain acyl-coa dehydrogenase protects mitochondria from lipid peroxidation in glioblastoma. *Cancer Discovery*. 2021;11:2904–23.
 66. Mbah NE, Lyssiotis CA. Metabolic regulation of ferroptosis in the tumor

- microenvironment. *Journal of Biological Chemistry*. 2022;298:101617.
67. Heydt Q, Larrue C, Saland E, Bertoli S, Sarry JE, Besson A, et al. Oncogenic FLT3-ITD supports autophagy via ATF4 in acute myeloid leukemia. *Oncogene*. 2018;37:787–97.
68. Rysman E, Brusselmans K, Scheys K, Timmermans L, Derua R, Munck S, et al. De novo lipogenesis protects cancer cells from free radicals and chemotherapeutics by promoting membrane lipid saturation. *Cancer Research*. 2010;70:8117–26.
69. de Groot S, Lugtenberg RT, Cohen D, Welters MJP, Ehsan I, Vreeswijk MPG, et al. Fasting mimicking diet as an adjunct to neoadjuvant chemotherapy for breast cancer in the multicentre randomized phase 2 DIRECT trial. *Nature Communications*. 2020;11.
70. Lien EC, Westermark AM, Zhang Y, Yuan C, Li Z, Lau AN, et al. Low glycaemic diets alter lipid metabolism to influence tumour growth. *Nature*. 2021;599:302–7.
71. Stockwell BR, Friedmann Angeli JP, Bayir H, Bush AI, Conrad M, Dixon SJ, et al. Ferroptosis: A Regulated Cell Death Nexus Linking Metabolism, Redox Biology, and Disease. *Cell*. 2017;171:273–85.
72. Chen X, Kang R, Kroemer G, Tang D. Broadening horizons: the role of ferroptosis in cancer. *Nat Rev Clin Oncol*. 2021;18:280–96.
73. Lei G, Zhuang L, Gan B. Targeting ferroptosis as a vulnerability in cancer. *Nat Rev Cancer*. 2022;22:381–96.
74. Eaton JK, Furst L, Ruberto RA, Moosmayer D, Hilpmann A, Ryan MJ, et al. Selective covalent targeting of GPX4 using masked nitrile-oxide electrophiles. *Nat Chem Biol*. 2020;16:497–506.
75. Pardieu B, Pasanisi J, Ling F, Dal Bello R, Penneroux J, Su A, et al. Cystine uptake inhibition potentiates front-line therapies in acute myeloid leukemia. *Leukemia*. 2022;36:1585–95.
76. Cluzeau T, Sebert M, Rahmé R, Cuzzubbo S, Lehmann-Che J, Madelaine I, et al. Eprentapopt plus azacitidine in TP53-mutated myelodysplastic syndromes and acute myeloid Leukemia: A phase II study by the groupe francophone des Myélodysplasies (GFM). *Journal of Clinical Oncology*. *J Clin Oncol*; 2021. page 1575–83.
77. Tesfay L, Paul BT, Konstorum A, Deng Z, Cox AO, Lee J, et al. Stearoyl-CoA desaturase 1 protects ovarian cancer cells from ferroptotic cell death. *Cancer Research*. 2019;79:5355–66.
78. Hospital M-A, Jacquelin A, Mazed F, Saland E, Larrue C, Mondesir J, et al. RSK2 is a new Pim2 target with pro-survival functions in FLT3-ITD-positive acute myeloid leukemia. *Leukemia*. 2018;32:597–605.
79. Chen EY, Tan CM, Kou Y, Duan Q, Wang Z, Meirelles G V., et al. Enrichr: Interactive and collaborative HTML5 gene list enrichment analysis tool. *BMC Bioinformatics*. 2013;14.
80. Kuleshov M V., Jones MR, Rouillard AD, Fernandez NF, Duan Q, Wang Z, et al. Enrichr: a comprehensive gene set enrichment analysis web server 2016 update. *Nucleic acids research*. *Nucleic Acids Res*; 2016;44:W90–7.
81. Xie Z, Bailey A, Kuleshov M V., Clarke DJB, Evangelista JE, Jenkins SL, et al. Gene Set Knowledge Discovery with Enrichr. *Current Protocols*. John Wiley & Sons, Ltd; 2021;1:e90.
82. Subramanian A, Tamayo P, Mootha VK, Mukherjee S, Ebert BL, Gillette MA, et al. Gene set enrichment analysis: A knowledge-based approach for interpreting genome-wide expression profiles. *Proceedings of the National Academy of Sciences of the United States of America*. 2005;102:15545–50.
83. Mootha VK, Lindgren CM, Eriksson KF, Subramanian A, Sihag S, Lehar J, et al. PGC-1 α -responsive genes involved in oxidative phosphorylation are coordinately

- downregulated in human diabetes. *Nature Genetics*. Nature Publishing Group; 2003;34:267–73.
84. Dobin A, Davis CA, Schlesinger F, Drenkow J, Zaleski C, Jha S, et al. STAR: ultrafast universal RNA-seq aligner. *Bioinformatics*. 2013;29:15–21.
85. Sonesson C, Love MI, Robinson MD. Differential analyses for RNA-seq: transcript-level estimates improve gene-level inferences [Internet]. *F1000Research*; 2016 [cited 2023 Jan 7]. Available from: <https://f1000research.com/articles/4-1521>
86. Love MI, Huber W, Anders S. Moderated estimation of fold change and dispersion for RNA-seq data with DESeq2. *Genome Biology*. 2014;15:550.
87. Ritchie ME, Phipson B, Wu D, Hu Y, Law CW, Shi W, et al. limma powers differential expression analyses for RNA-sequencing and microarray studies. *Nucleic Acids Research*. 2015;43:e47.
88. Subramanian A, Tamayo P, Mootha VK, Mukherjee S, Ebert BL, Gillette MA, et al. Gene set enrichment analysis: A knowledge-based approach for interpreting genome-wide expression profiles. *Proceedings of the National Academy of Sciences*. *Proceedings of the National Academy of Sciences*; 2005;102:15545–50.
89. Yu G, Wang L-G, Han Y, He Q-Y. clusterProfiler: an R package for comparing biological themes among gene clusters. *OMICS*. 2012;16:284–7.
90. Meerbrey KL, Hu G, Kessler JD, Roarty K, Li MZ, Fang JE, et al. The pINDUCER lentiviral toolkit for inducible RNA interference in vitro and in vivo. *Proceedings of the National Academy of Sciences of the United States of America*. *Proc Natl Acad Sci U S A*; 2011;108:3665–70.
91. Campeau E, Ruhl VE, Rodier F, Smith CL, Rahmberg BL, Fuss JO, et al. A versatile viral system for expression and depletion of proteins in mammalian cells. *PLoS ONE*. *PLoS One*; 2009;4.
92. Ianevski A, Giri AK, Aittokallio T. SynergyFinder 2.0: visual analytics of multi-drug combination synergies. *Nucleic Acids Research*. Oxford Academic; 2020;48:W488–93.
93. Adoue V, Binet B, Malbec A, Fourquet J, Romagnoli P, van Meerwijk JPM, et al. The Histone Methyltransferase SETDB1 Controls T Helper Cell Lineage Integrity by Repressing Endogenous Retroviruses. *Immunity*. 2019;50:629–644.e8.
94. Ackermann AM, Wang Z, Schug J, Naji A, Kaestner KH. Integration of ATAC-seq and RNA-seq identifies human alpha cell and beta cell signature genes. *Molecular Metabolism*. Elsevier GmbH; 2016;5:233–44.
95. Buenrostro J, Wu B, Chang H, Greenleaf W. ATAC-seq method. *Current Protocols in Molecular Biology*. 2016;2015:1–10.
96. Buenrostro JD, Giresi PG, Zaba LC, Chang HY, Greenleaf WJ. Transposition of native chromatin for fast and sensitive epigenomic profiling of open chromatin, DNA-binding proteins and nucleosome position. *Nature Methods*. 2013;10:1213–8.
97. Tsompana M, Buck MJ. Chromatin accessibility: A window into the genome. *Epigenetics and Chromatin*. 2014;7:1–16.
98. Zheng GXY, Terry JM, Belgrader P, Ryvkin P, Bent ZW, Wilson R, et al. Massively parallel digital transcriptional profiling of single cells. *Nature Communications*. 2017;8.
99. Hao Y, Hao S, Andersen-Nissen E, Mauck WM, Zheng S, Butler A, et al. Integrated analysis of multimodal single-cell data. *Cell*. Elsevier B.V.; 2021;184:3573–3587.e29.
100. Hafemeister C, Satija R. Normalization and variance stabilization of single-cell RNA-seq data using regularized negative binomial regression. *Genome Biology*. 2019;20.
101. Stuart T, Butler A, Hoffman P, Hafemeister C, Papalexi E, Mauck WM, et al. Comprehensive Integration of Single-Cell Data. *Cell*. Cell Press; 2019;177:1888–1902.e21.
102. Tirosh I, Izar B, Prakadan SM, Wadsworth MH, Treacy D, Trombetta JJ, et al. Dissecting the multicellular ecosystem of metastatic melanoma by single-cell RNA-seq. *Science*. American Association for the Advancement of Science; 2016;352:189–96.

103. Seyer A, Boudah S, Broudin S, Junot C, Colsch B. Annotation of the human cerebrospinal fluid lipidome using high resolution mass spectrometry and a dedicated data processing workflow. *Metabolomics*. *Metabolomics*; 2016;12.
104. Kessner D, Chambers M, Burke R, Agus D, Mallick P. ProteoWizard: Open source software for rapid proteomics tools development. *Bioinformatics*. *Bioinformatics*; 2008;24:2534–6.
105. Giacomoni F, Le Corguillé G, Monsoor M, Landi M, Pericard P, Pétéra M, et al. Workflow4Metabolomics: A collaborative research infrastructure for computational metabolomics. *Bioinformatics*. *Bioinformatics*; 2015;31:1493–5.
106. Bligh EG, Dyer WJ. A rapid method of total lipid extraction and purification. *Canadian journal of biochemistry and physiology*. *Can J Biochem Physiol*; 1959;37:911–7.
107. Millard P, Delépine B, Guionnet M, Heuillet M, Bellvert F, Létisse F. IsoCor: Isotope correction for high-resolution MS labeling experiments. *Bioinformatics*. *Oxford Academic*; 2019;35:4484–7.
108. Bankhead P, Loughrey MB, Fernández JA, Dombrowski Y, McArt DG, Dunne PD, et al. QuPath: Open source software for digital pathology image analysis. *Sci Rep*. *Nature Publishing Group*; 2017;7:16878.

Figure 1. FLT3-mutant AML cells exhibit increased lipid biosynthesis dependent on C/EBP α . **A**, Experimental scheme of *in vivo* amplification of FLT3-ITD primary samples from patients with AML by serial transplantation in NSG mice (n=3). Human leukemic cells were sorted from mice bone marrow samples using hCD33/hCD45 staining, and incubated *ex vivo* with vehicle or 10nM quizartinib (QUIZ) during 6h before processing RNA samples for transcriptomics. *Bottom panel* represent the evolution of the ratio between FLT3-ITD mutation and its non-mutated counterpart during serial transplantation of PDX samples in NSG mice. **B**, Differential gene expression (DGE) analysis using microarrays in patient-derived AML cells incubated with vehicle or 10nM QUIZ for 6h was analyzed using Gene Set Enrichment Analysis (GSEA) of Hallmark 2020, Biological Process (GO) and REACTOME gene sets (Normalized Enrichment Score, NES (vehicle vs QUIZ), p-value<0.05). **C**, Schematic representation of AML PDX treatment by GILT given by oral gavage. Six different PDXs were treated with vehicle or 30mg/kg/day GILT (n=4-19 mice in each group) for 7 days. One PDX (PDX^{TUH93}) was also treated during 14 days. **D**, Targeted next generation sequencing of samples from AML patients used to perform *ex vivo* and *in vivo* PDX assays. Mutations in *NPM1*, *IDH1*, *IDH2*, *DNMT3A*, *TET2*, *STAG2*, *WT1*, *CEBPA* and *FLT3* searched among a panel of 41 genes are reported. Presence of FLT3-ITD and FLT3-TKD are specified. French-American-British (FAB) subtypes are provided. **E**, Number of viable CD33⁺/CD45⁺ human AML cells in bone marrow and spleen of six AML PDXs in vehicle and GILT groups. Fold-changes (FC) between the mean number of leukemic cells in vehicle and GILT groups are provided. **F**, Differential gene expression (DGE) analysis using microarrays in vehicle- or GILT-treated PDXs and using GSEA of Hallmark 2020, Biological Process (GO) and REACTOME gene sets (NES (vehicle vs GILT), p-value<0.05). **G**, MOLM-14 and MV4-11 cell lines were incubated with vehicle or 3nM QUIZ for 14h. Quantitative proteomic analysis using liquid chromatography electrospray ionization tandem mass spectrometry (LC-ESI-MS/MS) was performed on these samples. FC and false discovery rate (FDR) q-values for vehicle versus QUIZ comparisons are provided (n=3). Proteins involved in lipid biosynthetic pathways are highlighted in red. **H and I**, Primary FLT3-ITD AML cells were incubated with vehicle or 10nM QUIZ for 14h. Western blots on total protein extracts were done using anti-C/EBP α , SREBP1 (t-SREBP1 and m-SREBP1: total and mature SREBP1, respectively), FADS2, SCD and actin antibodies (**H**) and quantified (**I**). **J**, Schematic diagram of ATACseq design

and comparison. **K**, Peak density heatmap of ATAC-seq reads for shCTL (n=2) and shC/EBP α (n=2) peaks in FLT3-ITD AML cells in region of 4kb surrounding peak centers. **L**, Venn diagram of nearest genes depleted in shC/EBP α MOLM14 cells and downregulated protein in MOLM14 cells upon QUIZ. **M**, Example of track view of the *SCD* locus showing ATAC-seq results for shC/EBP α (green track) and shCTL (black track) in MOLM14 AML cells, with regions of differential accessibility (BedTools intersect) depicted in red. Vertical bars indicate standard deviations. *: p<0.05; **: p<0.01; ***: p<0.001.

Figure 2. Activation of the FLT3-C/EBP α axis is associated with lipid biosynthetic pathways. **A**, Generation of a *CEBPA_UP* signature by the intersection of genes downregulated after *CEBPA* depletion (comparison between cells transduced with anti-*CEBPA* (two different sequences) or CTL constitutive shRNAs; FC<0.77, FDR and q-value<0.05) and upregulated after *CEBPA* overexpression (comparison between cells transduced with *CEBPA*-OE and empty vector; FC>1.3, FDR and q-value<0.05). **B**, Enrichr online software was used to analyze the Hallmark 2020 gene signatures enriched in *CEBPA_UP* signature (p-value<0.05). **C**, Enrichment analysis of the *CEBPA_UP* signature in DEG analysis between vehicle- and QUIZ-treated PDX AML samples (*upper panel*) and between FLT3-ITD versus FLT3 non-mutated (WT for wild type) samples from the TCGA cohort (*lower panel*). **D**, Intersection between *CEBPA_UP* and FLT3-ITD-UP PDX and cell lines signatures revealing six commonly modulated genes. **E**, Schematic representation of single-cell RNA sequencing (scRNAseq) assays done in AML PDXs treated *in vivo* with vehicle or GILT. AML cells were collected from three different PDXs (PDX^{TUH93}, PDX^{TUH84}, PDX^{TUH110}) before and after GILT treatment. Human CD33⁺/CD45⁺ AML cells were sorted, and single-cell transcriptome was generated using 10X Genomics technology. Single cells were clustered, and gene signature and single gene enrichment analysis were performed. **F**, Uniform manifold approximation and projection (UMAP) plot of 5,395 cells from PDX^{TUH93} using Seurat. Colors indicate clusters derived with the Louvain Algorithm in Seurat. **G**, UMAP plot colored by treatment condition (vehicle: n=1,792 cells; GILT D14: n=3,465 cells). **H**, Proportion of each condition per cluster from PDX^{TUH93}. **I-J**, Visualization on the UMAP plot of FLT3-ITD-UP cell line signature (**I**) and *CEBPA_UP* signature (**J**) enrichment in

vehicle- compared to GILT-treated PDX^{TUH93}. **K**, Heatmap showing the expression of each gene per cell in vehicle- compared to GILT-treated PDX^{TUH93}. Dendrograms represent the hierarchical clustering of cells (*left*) and genes (*bottom*). Cluster identities are shown on the right of the Heatmap. **L**, Visualization on the UMAP plot of *SCD* co-expressed genes enrichment in vehicle- compared to GILT-treated PDX^{TUH93}.

Figure 3. *C/EBP*α regulates rate-limiting lipid biosynthetic enzymes downstream of *FLT3-ITD*. **A**, Bulk RNAseq performed on bone marrow (22) or blood (19) specimens from patients with *FLT3*-mutant AML collected before (n=20) or during (n=21) GILT therapy. Four samples experienced technical failures in the post-GILT group. Patients were stratified in two group based on on the evolution of *CEBPA_UP* signature during GILT treatment: enriched (group 1) versus stable/depleted (group 2) post-GILT. **B-C**, Enrichment of *CEBPA_UP*, *FLT3-ITD_UP* and *MKI67* gene signatures during GILT therapy in the patient group 1. **D-E**, MOLM-14 cells transduced with doxycycline (dox)-inducible control (CTL) or anti-*CEBPA* shRNAs and seeded with 1µg/ml dox during 3 days. **D**, Western blots were done with anti-*C/EBP*α, *SCD*, *FASN*, *FADS2* and actin antibodies. **E**, Cells were incubated with 2nM QUIZ or 25nM GILT for 24h and cell viability was assessed by annexin V staining. **F**, MOLM-14 cells expressing dox-inducible anti-*CEBPA* or CTL shRNAs were transplanted to NSG mice, which were given 0.2mg/ml dox in drinking water from the day 7 (CLDX#1) or 10 (CLDX#2) of transplant. Two weeks after transplant, mice were sacrificed, and leukemia propagation was investigated. **G**, Two independent cell line-derive xenograft (CLDX) assays were performed as indicated (n=8 mice in each). Tumor burden was measured using human CD45 staining (*left panel*) and the proportion of efficiently-transduced RFP⁺ viable cells among hCD45⁺ cells was evaluated (*right panel*). **H-J**, MOLM-14 cells were transduced with a dox-inducible vector allowing *CEBPA* overexpression (OE), or with the empty vector. **H**, Western blot in exctacts collected after 48h incubation with dox using antibodies against *C/EBP*α, *SCD*, *FASN*, *FASD2* and actin. **I**, Cells were incubated with dose-range QUIZ for 48h and viability was assessed by a luminescence-based cell viability assay (Alamar Blue). **J**, Viability by annexin V staining in cells incubated with 3nM QUIZ for 48h. **K**, MOLM-14 cells were transduced with GFP⁺ empty or *CEBPA*-OE vectors and

transplanted to NSG mice. After two weeks, mice were sacrificed and tumor burden and differentiation were measured by hCD45 and CD14/CD15 staining, respectively. **L**, MOLM-14 cells were transduced with dox-inducible wild type (WT), S21A (Serine to Alanine substitution, non phosphomimetic) or S21D (Serine to Aspartic acid substitution, phosphomimetic) *CEBPA* forms. After dox induction during 72h, cells were treated with vehicle, 3nM QUIZ or 30nM GILT for 48h and cell viability was measured by DRAQ7 staining. Vertical bars indicate standard deviations. *: p<0.05; **: p<0.01; ***: p<0.001.

Figure 4. C/EBP α drives fatty acid biosynthetic fluxes in FLT3-mutant leukemic cells. **A**, Global lipidomics in MOLM-14 cells depleted from C/EBP α (siRNA 24h, dox-inducible shRNA or constitutive shRNA 72h) or overexpressing C/EBP α (dox-inducible 72h) and treated with vehicle or 3nM QUIZ for 14h. PC/PC-P/PC-O: phosphatidylcholine/-plasmogen/-alkyl ether; PE/PE-P/PE-O: phosphatidylethanolamine/-plasmogen/-alkyl ether; PG: phosphatidylglycerol; LPC: lysophosphatidylcholine; LPE: lysophosphatidylethanolamine; SM: sphingomyelin; CER: ceramide; HexCER: hexosylceramide; TG: triacylglyceride. **B**, Schematic representation of carbon atom (circles) transitions and tracers used to detect labeled FAs. Isotopic label from [U-¹³C]-glucose (red) or [U-¹³C]-glutamine (blue) to FAs synthesis through Pyruvate Carboxylase (PC; pink) or Pyruvate DeHydrogenase (PDH; orange), tricarboxylic acid (TCA) cycle (blue), or reductive glutamine metabolism (green). Pyr: pyruvate; AcCoA: acetyl-CoA; Cit: citrate; α -KG: α -ketoglutarate; Mal: malate; OOA: oxaloacetate; ACLY: ATP citrate lyase; FASN: Fatty acid synthase; Glu: glutamate. **C-D**, MOLM-14 seeded with [U-¹³C]-glucose- or [U-¹³C]-glutamine-containing medium and treated with vehicle or 2nM QUIZ for 24h. **(C)** Percentage of ¹³C enrichment in C_{14:0}, C_{16:0}, C_{16:1}, C_{18:0} and C_{18:1} total FA. **(D)** Isotopologue distribution in C_{14:0}, C_{16:0}, C_{16:1}, C_{18:0} and C_{18:1} total FA. The quantification of each isotopologue was normalized to the amount of proteins and cell number for each condition, separately. Vertical bars indicate standard deviations. *: p<0.05; **: p<0.01; ***: p<0.001.

Figure 5. FLT3 inhibition decreases mono-unsaturated fatty acid dependent on C/EBP α . **A**, Schematic representation of FA synthesis pathways. FASN: fatty Acid Synthase; SCD: Steroyl-CoA Desaturase; FADS: Fatty Acid Desaturase; ELOVL: Elongation of very long chain fatty acids protein; SFA: saturated fatty acid; MUFA: mono-unsaturated fatty acid; PUFA: polyunsaturated fatty acid; Lipid-ROS: lipid peroxides; PL: phospholipids; FA: fatty acid; TG: triglyceride. **B-D**, Targeted lipidomics showing repartition of SFAs, MUFAs and PUFAs distribution into phosphoethanolamine (PE) (**B**) and phosphatidylcholine (PC) (**C**) in C/EBP α -depleted MOLM-14 compared to control, CEBPA-OE compared to empty MOLM-14, empty MOLM-14 incubated with vehicle or 3nM QUIZ for 14h, and CEBPA-OE MOLM-14 incubated with vehicle or 3nM QUIZ for 14h (from the left to the right, respectively). PUFA:MUFA ratio for PC and PE are shown in (**D**). Vertical bars indicate standard deviations. ns: not significant; *: p<0.05; **: p<0.01; ***: p<0.001.

Figure 6. Inhibition of SCD-dependent mono-unsaturated FA biosynthesis sensitizes FLT3i-treated AML cells to ferroptotic cell death. **A**, FLT3 inhibition led to decreased MUFA through SCD inhibition. Resulting increased PUFA/MUFA ratio favored lipid-ROS formation, which can be further promoted by SCD or GPX4 inhibition by MF-438 and RSL3, respectively, to drive ferroptotic cell death. In contrast, the lipid-ROS scavenger Ferrostatin-1 prevents ferroptotic cell death. **B-C**, MOLM-14 or MV4-11 cells supplemented with or without oleate were incubated with vehicle or 125nM (**B**) and 250nM RSL3 (**C**). Lipid peroxidation was measured by C11-Bodipy staining after 12h-treatment (**B**) and cell viability measured by PI staining after 24h-treatment (**C**). **D-E**, MOLM-14 and MV4-11 cells were transduced with dox-inducible vector for SCD overexpression (SCD-OE). (**D**) Western blot using SCD and actin antibodies. (**E**) MV4-11 cells expressing empty vector or SCD-OE were incubated with QUIZ as indicated and cell viability was measured using PI staining. **F**, Cell viability assays using Alamar Blue in MOLM-14 (*left panel*) and MV4-11 (*right panel*) cells overexpressing SCD (SCD-OE) or the empty vector, and incubated with dose-range RSL3 for 14h, and with vehicle or 10 μ M Ferrostatin-1 (Fer-1). **G-H**, Empty vector or SCD-OE MOLM-14 and MV4-11 cells were incubated with vehicle or 250-500nM RSL3. Lipid peroxidation measured by C11 Bodipy staining after 12h-treatment (**G**) and cell viability assays using PI staining after 24h-treatment (**H**). **I-K**, MOLM-14 and

MV4-11 cells were transduced with constitutive shRNAs against *SCD* (shSCD#1 and shSCD#2) or shCTL. **I**, Western blots done 48h after transduction with *SCD* and actin antibodies. **J-K**, MOLM-14 and MV4-11 cells transduced with CTL or anti-*SCD* shRNAs were incubated with 100nM RSL3. Lipid peroxidation measured by C11-Bodipy staining after 12h-treatment (**J**) and cell viability assessed by PI staining after 24h-treatment (**K**). **L**, Primary AML patient samples (n=3; PDX^{TUH06} PDX^{TUH84}, PDX^{TUH93}) and FLT3-ITD AML cell lines (MOLM-14 and MV4-11) were incubated with crossed dose-range QUIZ and MK-436 for 24h. Cell viability was measured using a luminescence-based assay (Alamar Blue) and results are expressed as a ratio to the untreated condition for each well in a viability matrix (top panel) and using synergy maps using zero interaction potency (ZIP) synergy scores and a threshold ZIP>10 considered as significant (bottom panel). Vertical bars indicate standard deviations. *: p<0.05; **: p<0.01; ***: p<0.001.

Figure 7. FLT3 inhibition primes FLT3-mutant leukemic cells to ferroptotic cell death. **A** MOLM-14 cells in which C/EBP α was depleted or overexpressed were incubated with vehicle or 100nM or 250nM RSL3 respectively for 24h. **B**, Lipid peroxidation measured using C11-Bodipy staining in MOLM-14 and MV4-11 cells treated with vehicle or FLT3i (3nM and 10nM QUIZ or 30nM and 100nM GILT, respectively), and vehicle or 100nM RSL3 for 12h. **C**, Cell viability assessed by PI staining in MOLM-14 and MV4-11 cells treated with vehicle or FLT3i (3nM QUIZ or 30nM GILT), and vehicle or 100nM RSL3 for 24h. **D**, Patient-derived AML samples (n=3) were incubated *ex vivo* with crossed dose-range QUIZ and RSL3 for 48h. Cell viability was measured using a luminescence-based assay (Alamar Blue) and results are expressed as a ratio to the untreated condition for each wheel in a viability matrix (*top panel*) and using synergy maps using zero interaction potency (ZIP) synergy scores and a threshold ZIP>10 considered as significant (*bottom panel*). **E**, MOLM-14 cells were invalidated for *GPX4* using CRISPR-Cas9, and cultured with 10 μ M Fer-1. Cell viability (using PI staining) and lipid peroxidation (using C¹¹ Bodipy staining) were measured without or with Fer-1 dependent on time. **F-J**, MOLM-14 cells were transduced with CTL or *GPX4*-targeting CRISPR-Cas9 vectors, and cultured with 10 μ M Fer-1 to avoid cell death induced by *GPX4* ablation (*GPX4*^{KO}). These cells were xenografted to immunodeficient NSG mice and treated *in vivo* with 10mg/kg/day

Fer-1 by intraperitoneal (IP) injection during 10 days. Then CTL and GPX4^{KO} groups were treated with vehicle or 10mg/kg/day GILT by oral gavage for 7 days before evaluation of tumor burden or follow-up for survival. Each group was made of 5-9 mice. **F**, Schematic overview of the experimental design. **G**, Staining with anti-4-HNE antibody in paraffine-embedded bone marrow specimens. *Right panel*: quantification. **H**, Quantification of human CD45⁺ leukemic cell burden at day 7. **I**, Proportion of human CD45⁺ cells at day 7. **J**, Survival curves. **K**. Schematic diagram of lipid metabolism reprogramming induced by C/EBP α in FLT3-ITD AML cells through SCD-FADS2-FASN at the steady state and upon inhibition of C/EBP α or treatment with FLT3i combined with ferroptosis inducers. Vertical bars indicate standard deviations. *: p<0.05; **: p<0.01; ***: p<0.001.

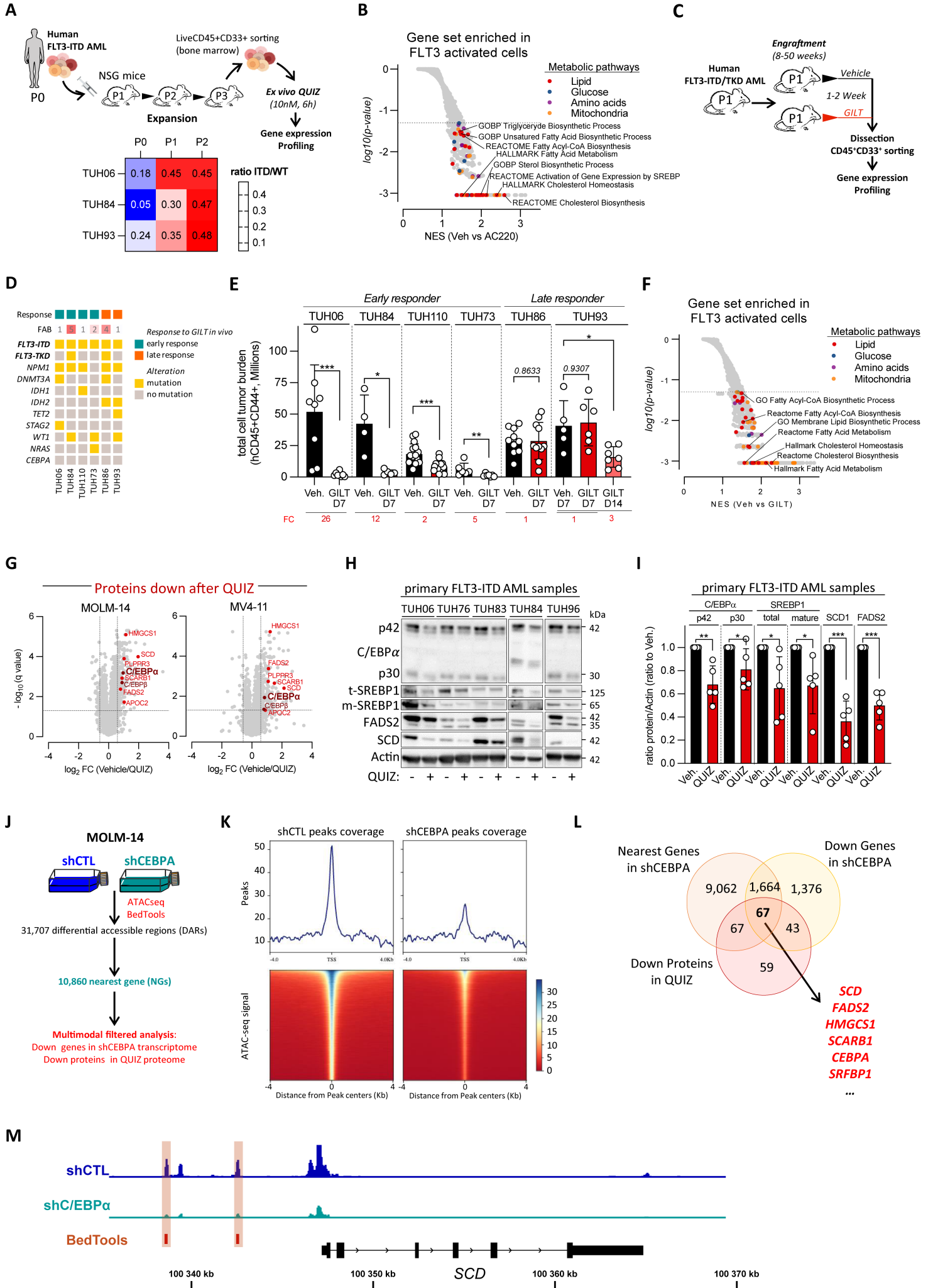


Figure 1

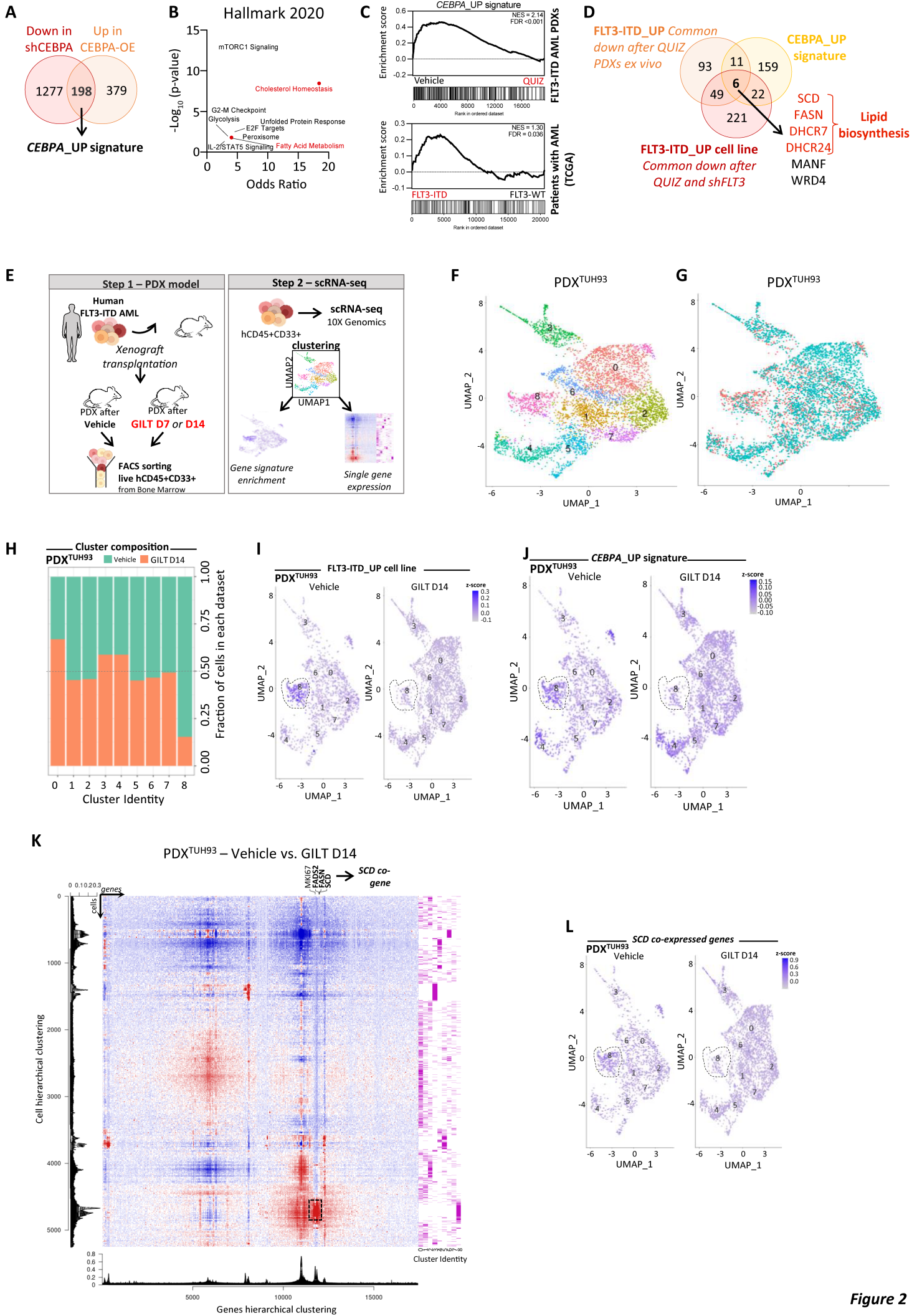


Figure 2

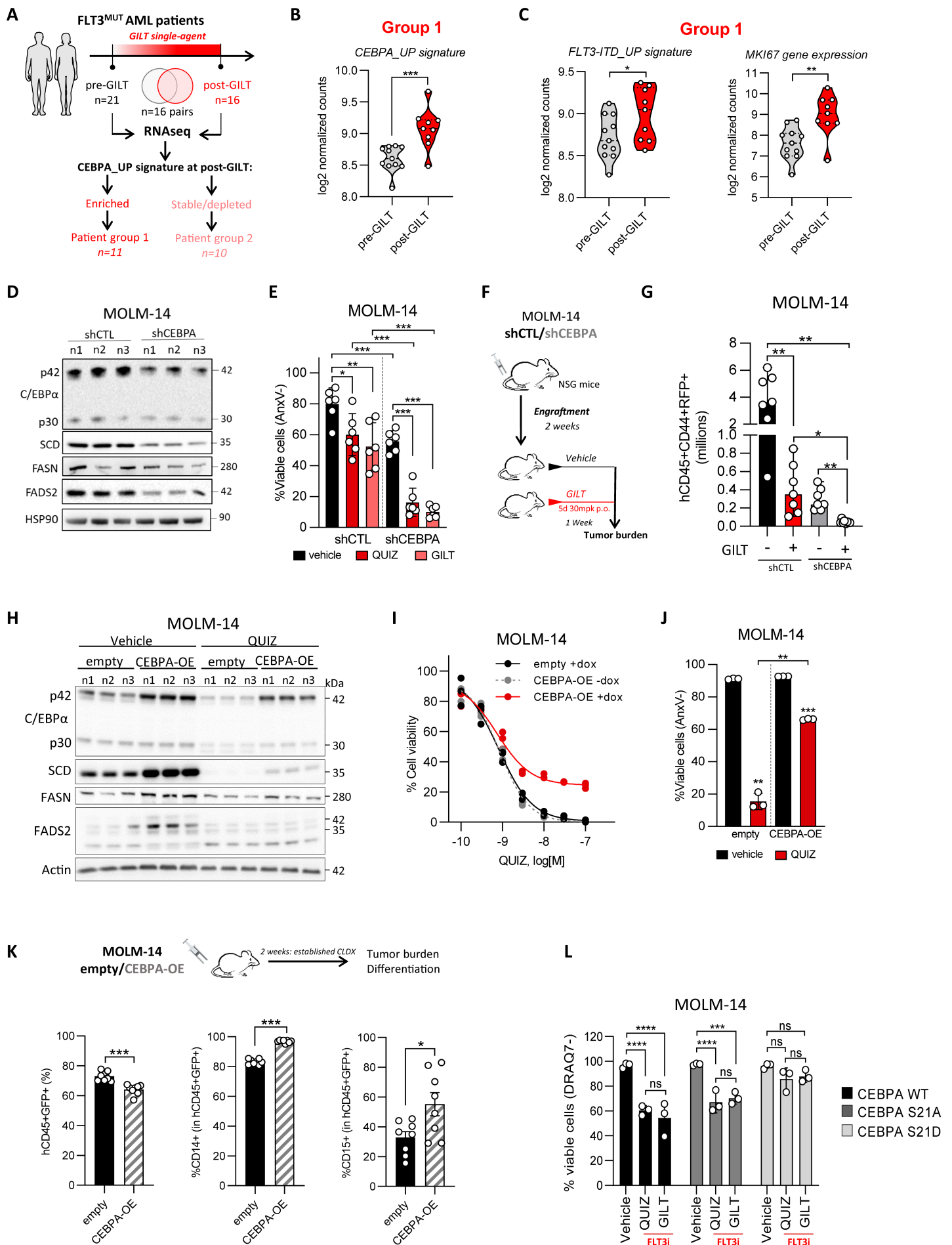
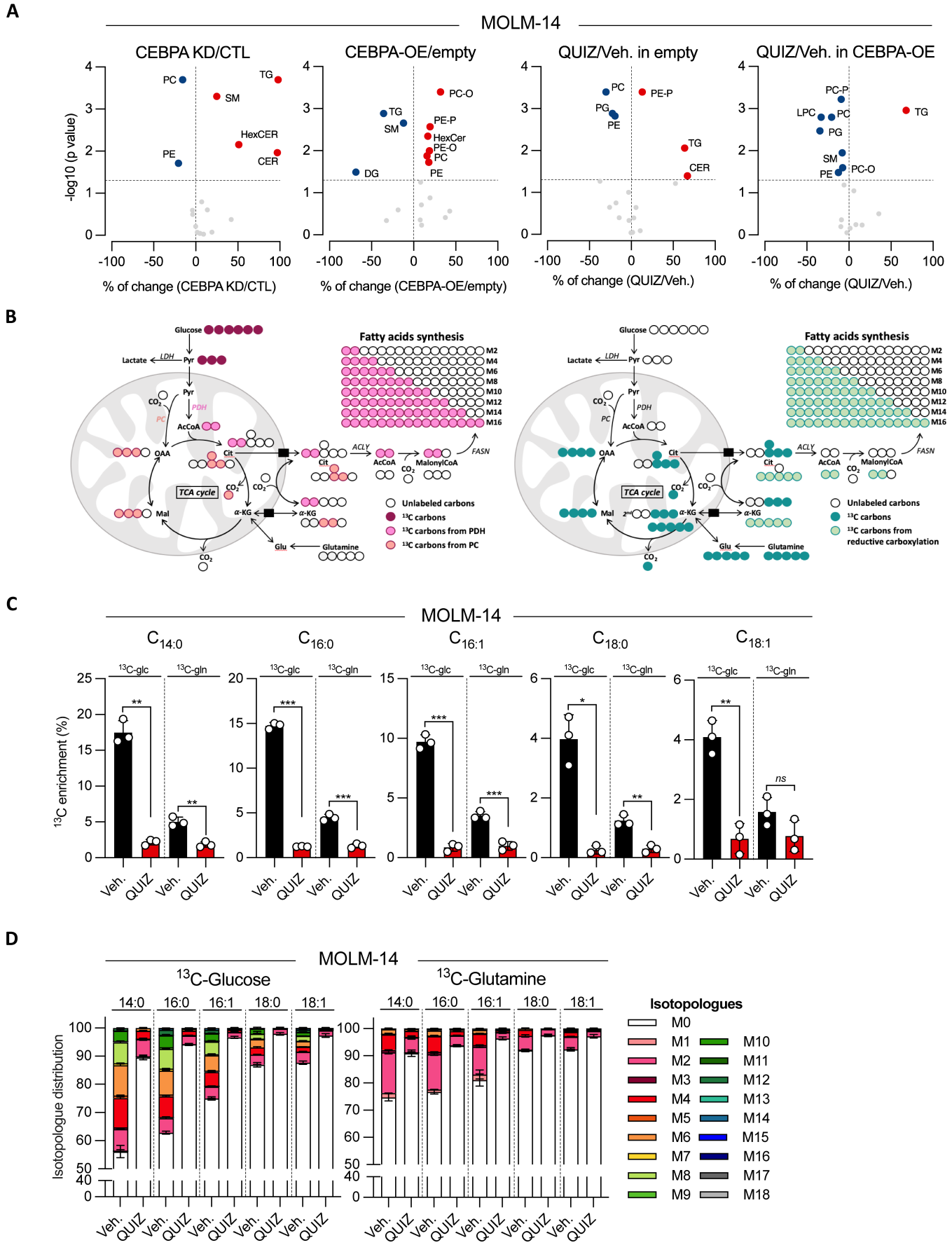


Figure 3



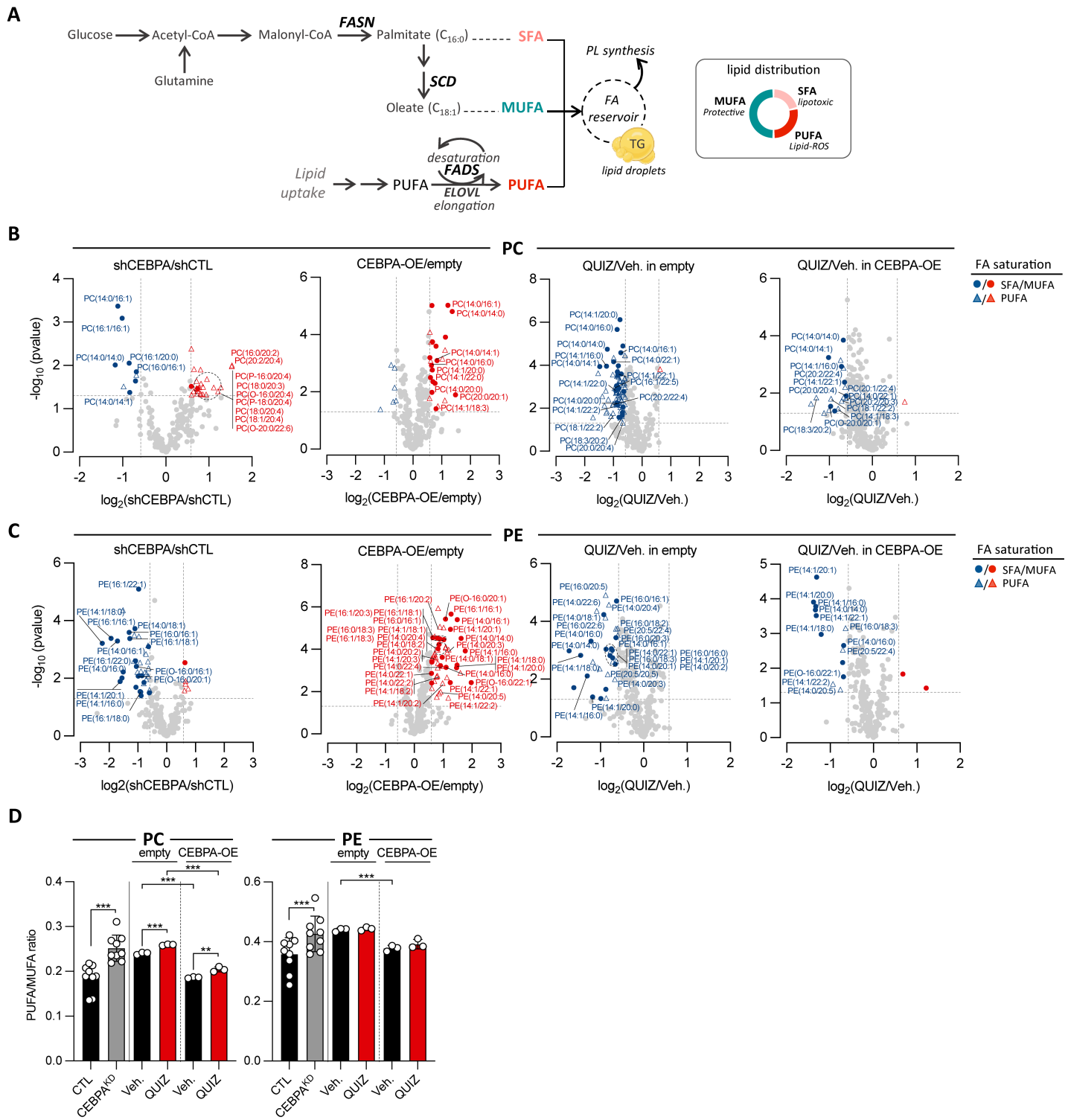


Figure 5

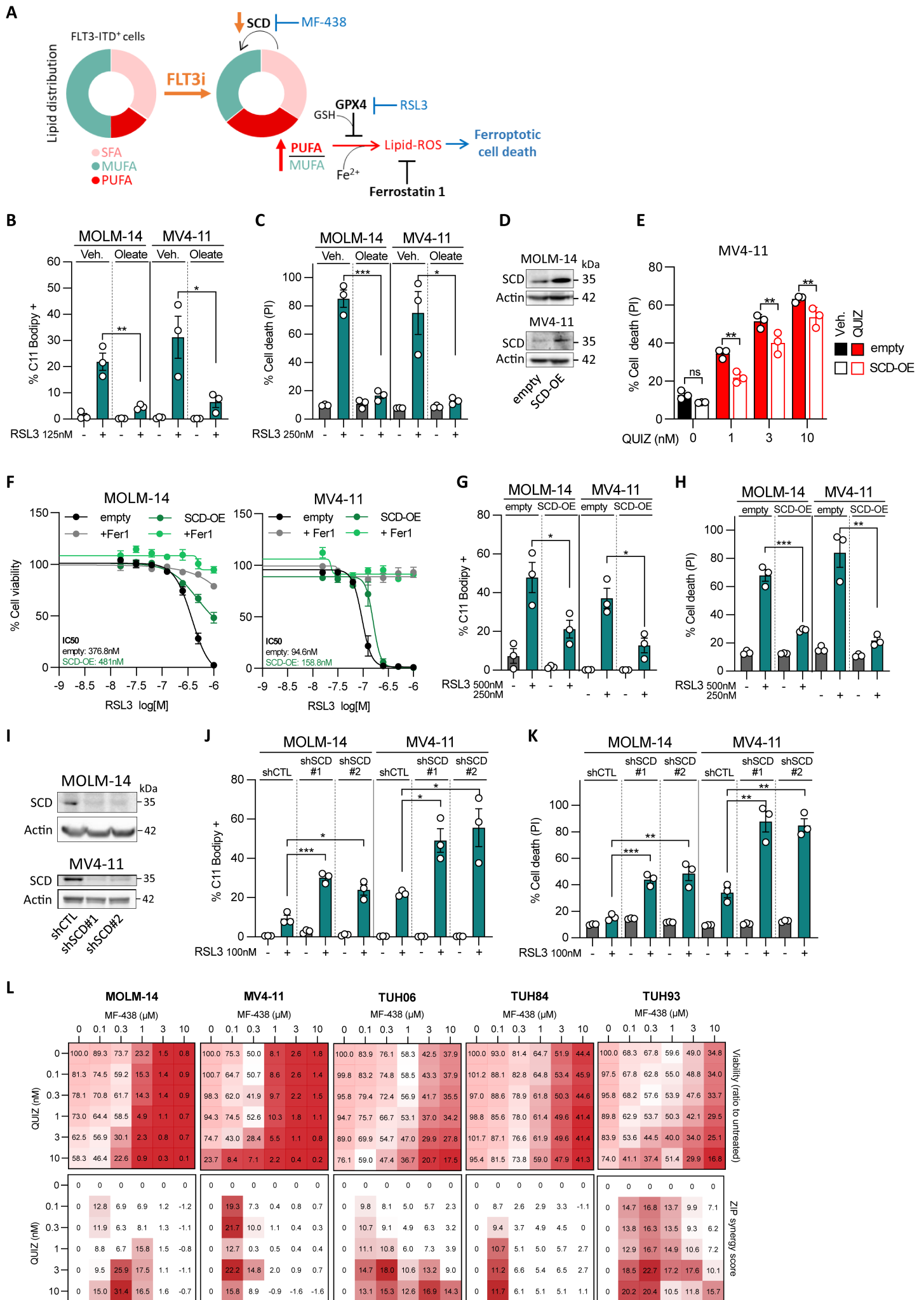


Figure 6

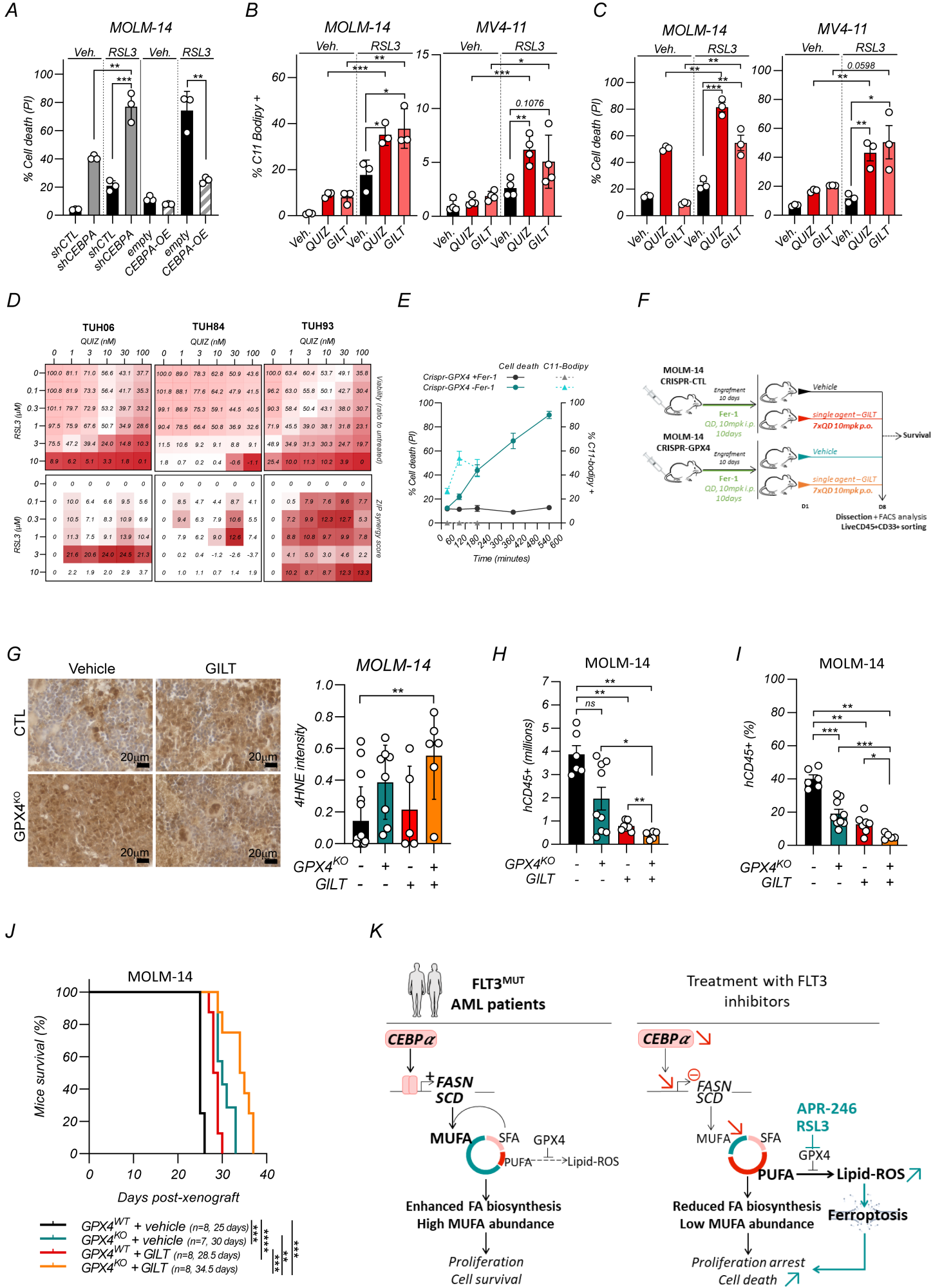


Figure 7